Atlantic Water Pathways and Associated Heat Transport at the Atlantic-Arctic Gates in Two Eddying Climate Models

Esteban Avella Shaw
Master of Science

Department of Atmospheric & Oceanic Sciences
McGill University
Montreal, Quebec, Canada

August 11, 2024

A thesis submitted to McGill University in partial fulfillment of the requirements of the degree of Master of Science

Abstract

The impact of horizontal resolution on the pathways of the Atlantic Waters (AW) to the Atlantic-Arctic gates, and their associated heat transport are investigated using two configurations of the GFDL CM2-O climate model suite, one at 1/10° (HighRes) and one at 1/4° (MedRes), run under a preindustrial scenario. Using 5-day averaged velocity fields from the configurations, an offline Lagrangian tracking experiment is conducted by initializing passive virtual particles with constant volume transport at 55°N within the precursors of the AW in the eastern Atlantic sector and following them until the Barents Sea Opening (BSO) and Fram Strait (FS). The majority of particles reaching the Atlantic-Arctic gates were found to originate east of 22°E and in the top 500 meters. A small fraction of the particles initialized deeper than 1000 meters reach the gates by upwelling along major topographic features, in particular around the Iceland Plateau. The two configurations were found to mainly differ by the partitioning of the AW between BSO and FS. While the majority of the particles reach BSO first in MedRes, they reach FS first in HighRes. This difference may be explained by two bifurcations of AW on the route to the Arctic. The first one is located South of Iceland and reroutes more particles towards the Irminger Current in HighRes than in MedRes. The second is located at about 70°N in the Norwegian Sea and reroutes more particles towards FS in HighRes than in MedRes. Differences in the pathways of AW between the two configurations are hypothesized to be caused by flow-topography interactions. The preference of AW for the FS pathway to the Arctic in HighRes results in a greater heat transport at that gate and a lower impact on the sea ice cover as the inflowing heat remains buried at depth, in contrast to MedRes which sees more heat penetrating at BSO and impacting the sea ice over the Barents Sea shelf. Our findings thus highlight that resolution may not only impact

the strength of the northward heat transport but also the pathways of that heat towards the Arctic, the latter being as important as the former in determining the sea ice cover.

Abrégé

L'impact de la résolution horizontale sur les trajectoires des eaux atlantiques (AW) vers les points d'entrée de l'Arctique, ainsi que le transport de chaleur leur étant associé, sont étudiés à l'aide de deux configurations de la suite de modèles de climat GFDL CM2-O, l'une à 1/10° (HighRes) et l'autre à 1/4° (MedRes), soumises à un scénario préindustriel. En utilisant les champs de vitesse moyennés sur 5 jours provenant des configurations, une expérience de suivi lagrangien post-simulation est réalisée en initialisant des particules virtuelles passives avec un transport volumique constant à 55°N au sein des eaux précurseuses des AW dans le secteur Atlantique oriental et en les suivant jusqu'au Détroit de la Mer de Barents (BSO) et le Détroit de Fram (FS). La majorité des particules atteignant ces détroits provient de l'est de 22°E et des 500 premiers mètres. Une petite fraction des particules initialisées à plus de 1000 mètres de profondeur atteint les passages en remontant le long des principales structures topographiques, en particulier autour du Plateau Islandais. Les deux configurations diffèrent principalement par la répartition des AW entre BSO et FS. Alors que la majorité des particules atteint d'abord BSO dans MedRes, elles atteignent d'abord FS dans HighRes. Cette différence pourrait être expliquée par deux bifurcations des AW sur leur route vers l'Arctique. La première est située au sud de l'Islande et redirige plus de particules vers le courant Irminger dans HighRes que dans MedRes. La seconde est située vers 70°N dans la Mer de Norvège et redirige plus de particules vers FS dans HighRes que dans MedRes. Les différences entre les deux configurations dans les routes empruntées par les AW pourraient être dues à la représentation des interactions courant-topographie. La préférence des AW pour la voie vers FS dans HighRes entraîne un transport de chaleur plus important à ce pas-

sage et un impact moindre sur la couverture de glace de mer, car la chaleur entrante reste enfouie en profondeur, contrairement à MedRes qui voit plus de chaleur pénétrer à BSO et affecter la glace de mer sur le plateau de la Mer de Barents. Nos résultats soulignent ainsi que la résolution peut non seulement impacter l'amplitude du transport de chaleur vers le nord, mais aussi les trajectoires de cette chaleur vers l'Arctique, cette dernière étant aussi importante que la première pour déterminer la couverture de glace de mer.

Contribution

This thesis is presented on the format of a research article (paper manuscript) that will be submitted to the *Journal of Climate* and will include the following authors: Esteban Avella Shaw, Carolina O. Dufour, Rym Msadek, Camille Lique and Noémie Planat. Esteban Avella Shaw performed the Lagrangian experiments, completed all the analyses and wrote the manuscript. Carolina Dufour conceived the study and contributed to the interpretation of the results and to the writing of the manuscript. Rym Msadek and Camille Lique contributed to the interpretation of the results. Noémie Planat contributed to identify and fix the bug on the Lagrangian tracking algorithm described in Appendix A. The simulations of the two model configurations used in this thesis were run at the Geophysical Fluid Dynamics Laboratory, Princeton, New Jersey, United States.

Acknowledgements

I could not have taken this journey without my supervisor, Prof. Carolina O. Dufour, to whom I am deeply grateful for her invaluable patience and feedback. I would also like to express my deepest appreciation to my collaborators, Dr. Rym Msadek and Dr. Camille Lique, for their guidance, insights, and feedback. Additionally, I am grateful to the members of my research group, Noémie Planat, Dr. Jan Rieck, and Dr. Mathilde Jutras, for their overall support and expertise. I am profoundly indebted to Prof. Erik van Sebille and Dr. Michael Denes for their invaluable assistance and the time they invested in fixing the Parcels algorithm bug. Furthermore, I extend my heartfelt gratitude to my examiner, Prof. Bruno Tremblay, for his valuable feedback and constructive criticism. This endeavor would not have been possible without the generous support from the Fonds de recherche du Québec – Nature et technologies.

Special thanks to my entire research group for their relevant comments and advice during our weekly meetings. I am also sincerely thankful to my friends and cohort members, Victorine Daubies, Madeleine Fol, Stéphanie Bergeron, and Benjamin Riot-Bretêcher, with whom I have shared both joyful and stressful moments over the past two years.

Lastly, I would be remiss if I did not mention my friends and family in Belgium. Their unwavering belief in me has kept my spirits high and my motivation strong throughout this process.

Contents

1 Introduction **1**

2 Methods **8**
2.1 Model and Simulations 8
2.1.1 The CM2-O climate model suite 8
2.1.2 Preindustrial simulations 10
2.2 Lagrangian tracking experiments 13
2.2.1 Experimental set up 13
2.2.2 Computation of volume and heat transport 17

3 Results **19**
3.1 Main and secondary pathways of Atlantic Waters from 55°N to the Arctic gates 19
3.2 Inflow of Atlantic Waters at the Atlantic-Arctic gates 24
3.2.1 Barents Sea Opening 24
3.2.2 Fram Strait 26
3.3 Origin of the Atlantic Waters at the Atlantic-Arctic gates 28
3.4 Advection timescales of Atlantic Waters to the Atlantic-Arctic gates 32
3.5 Volume and heat transports of Atlantic Waters at the gates 34
3.5.1 Contribution of Atlantic Waters at 55°N to the volume and heat transports at the Atlantic-Arctic gates 34
3.5.2 Variability of volume and heat transports at the gates 35
3.5.3 Origin of the heat pulse at Fram Strait 37

4 Discussion and Conclusion **40**

5 Appendices **56**
A Parcels bug fix 56
B Initialization schematic 62
C 20-year averaged velocity fields at the Atlantic-Arctic gates 63
D Exiting transport at the Atlantic-Arctic gates 64
E Initialization branches east and west of 22°W 65
F Velocity field at different depths in both configurations 66
G Mean potential temperature timeseries 67
H Upwelling hotspots and individual trajectories 68

List of Figures

1.1 Schematic of the North Atlantic and Nordic-Sea circulations. The red arrows represent warm water currents, and the blues ones cold water currents. [Norwegian Current (NC), East Greenland Current (EGC), Subarctic Front Current (SAFC), Central Iceland Basin Current (CIBC), East Reykjanes Current (ERC), Irminger Current (Irm), West Greenland Current (WGC), Subarctic Front (SAF)]. The lightblue and darkgreen lines represent the Barents Sea Opening and the Fram Strait respectively. (Modified from Fig. 3-34 in Fieux, 2017). 4

2.1 20-year averaged (a-c) potential temperature (θ), (d-f) salinity (S),(g-i) oxygen concentration (O_2), and (j-k) meridional velocity (v), and their respective isocontours (white/black contours) along 55°N, in the two model configurations and the observations. The observational fields are from the World Ocean Atlas 2009 (Antonov et al., 2010; Garcia et al., 2010; Locarnini et al., 2010). In the first two columns, the dashed red box delineates the initialization zone of virtual particles. The bathymetry in the last row is different as the velocities are located on the northeast corner of the gridcells, and not in the center of the gridcells as for the tracers. 11

2.2 Bathymetry of the HighRes configuration, with the location of the two gates of interest and of the line where particles are initialized before being advected. 13

3.1 Main pathways towards the Atlantic-Arctic gates and relative importance of gates. Colors indicate the fraction of the total particle transport across the Atlantic-Arctic gates (Barents Sea Opening and Fram Strait) at each 0.25° by 0.25° grid column over the whole experiment. Grid cells with high values correspond to columns which have been visited either by many particles or by relatively fewer particles that are associated with high transport. Numbers overlaid on the continent correspond to the preference of particles entering the Arctic to go through Fram Strait or Barents Sea Opening first, expressed in particle-transport and color-coded by gate. 20

3.2 Vertical distribution of entering particle-transport at (a-b) Barents Sea Opening and (c-d) Fram Strait in both configurations. For each gate, colors indicate the fraction of particle-transport across that gate over the whole experiment. Particle-transport is binned into bins of 0.25° by 10 m for Barents Sea Opening, and 0.25° by 100 m for Fram Strait. Grid cells with high values have been visited either by many particles or by relatively fewer particles that are associated with high transport. 25
3.3 Trajectories of particles reaching (a-b) Barents Sea Opening and (c-d) Fram Strait in the two model configurations, color-coded according to their depth category at the time of initialization. For the sake of clarity, each subplot only displays 2000 trajectories, with the number of trajectories per depth range proportional to the transport distribution in that same range. Pie charts show the contribution of each depth range to the total particle-transport at each gate. Note that trajectories are flagged based on the first gate they cross. Consequently, some particles that initially reach the Barents Sea Opening might later recirculate and subsequently reach the Fram Strait, and vice versa. This explains why some trajectories crossing the Barents Sea Opening (a-b) appear to cross the Fram Strait too, and inversely for the trajectories crossing the Fram Strait (c-d). 30
3.4 Mean depth gradient, expressed in meters vertically per kilometer horizontally, of particles initialized deeper than 1 km and reaching (a-b) Barents Sea Opening and (c-d) Fram Strait in the two model configurations. Red tints indicate upwelling (positive gradient) and blue tints indicate downwelling (negative gradient), at each 1° by 1° grid column. Note that trajectories are flagged based on the first gate they cross. Consequently, some particles that initially reach the Barents Sea Opening might later recirculate and subsequently reach the Fram Strait, and vice versa. This explains why some gradients nearby Fram Strait might be observed for the particles crossing the Barents Sea Opening first (a-b), and reciprocally for the gradients observed nearby Barents Sea Opening, for the particles crossing Fram Strait first (c-d). 31
3.5 Normalized probability density distribution of the age of the particles at the time they cross a gate, for each gate and configuration. The bins size is half a month. The grey vertical line corresponds to the distribution's median (Md) and the black vertical line corresponds to the distribution's mean (Mn). Note that the abrupt decline at about 9 years is set by the advection time used for particles. However, extending the advection time to 15 years does not significantly change the mean nor the median of the distribution. 33
3.6 Time series of (a-d) volume transport and (e-h) heat transport across each Atlantic-Arctic gate for the entire experiment in each model configuration. Light lines show particle transport computed every 5 days, while dark lines indicate 1-year running means. White areas represent the period used to calculate the averaged transports presented in Table 2.2. This period starts by adding the median age of particles at gate crossing (Fig. 3.5) to the first experiment year (year 181) and ends by adding the median age to the last year of particle initialization (year 190). 36

3.7 The North Atlantic Oscillation (NAO) index (red/blue; left y-axis) computed from the normalized monthly-averaged sea level pressure difference between the Azores Islands and Iceland binned seasonally for both configurations. Also depicted are the monthly averaged Eulerian northward volume transports (right y-axis) for the North Atlantic Current (yellow) and the Irminger Current (magenta). 39

5.1 Particle trajectories initialized north of Fram Strait at the surface and advected in 2-D: a) fieldset created with from_mom5() (velocity field rotation not included), b) fieldset created with from_mom5() and particles advected with an idealized velocity field strictly following constant latitudes, c) fieldset created with from_nemo() (velocity field rotation included), d) fieldset created with from_mom5() with velocity field rotation included in a custom advection kernel (Listing 5.1). The grey lines represent the 500 m, 1 km, and 2 km isobaths in the region. 57

5.2 Simplified schematic of the initialization at 55°N. The virtual particles are represented with blue dots while the area attributed to each particle for the sake of computing the associated transport (*particle-transport*) is represented by the blue rectangles. The initialization area is represented by the dashed red rectangle. 62

5.3 20-year averaged (a-b) zonal (u) and (c-d) meridional (v) velocity fields at the Barents Sea Opening and Fram Strait respectively. 63

5.4 Vertical distribution of exiting particle-transport at gates. For each gate, colors indicate the fraction of particle-transport across that gate over the whole experiment. Particle-transport is binned into bins of 0.25° by 10 m for Barents Sea Opening, and 0.25° by 100 m for Fram Strait. Grid cells with high values have been visited either by many particles or by relatively fewer particles that are associated with high transport. 64

5.5 Main pathways of the particles seeded within (a-b) the eastern and (c-d) the western branch towards the Atlantic-Arctic gates and relative importance of gates. Colors indicate the fraction of the total particle transport across the Atlantic-Arctic gates (Fram Strait and Barents Sea Opening) at each 0.25° by 0.25° grid column over the whole experiment. Grid cells with high values correspond to columns which have been visited either by many particles or by relatively fewer particles that are associated with high transport. Numbers overlaid on the continent correspond to the preference of particles entering the Arctic to go through Fram Strait or Barents Sea Opening first, expressed in particle-transport and color-coded by gate. 65

5.6 Sea velocities at (a-b) 5.03, (c-d) 98.6, and (e-f) 181 m depth in both configurations. 66

5.7 Time series of particles' mean potential temperatures when crossing (a-b) Barents Sea Opening and (c-d) Fram Strait for the duration of the entire experiment in each model configuration. Light lines represent the mean potential temperature of all particles crossing the gate during each 5-day window, while dark lines indicate the 1-year running means. White areas correspond to the periods used to calculate the average potential temperature, represented by the temperature value overlaid in each subplot. The beginning of the period is determined by adding the median of the normalized probability density distribution of the age of the particles at the time they cross a gate (Fig. 3.5) to the first year of the experiment (year 181). The end of the period is determined by adding the median to the last year of particles initialization (year 190). . 67
5.8 Mean depth gradient, expressed in meters vertically per kilometer horizontally, of particles initialized deeper than 1 km and reaching (a-b) Barents Sea Opening and (c-d) Fram Strait in the two model configurations. Red tints indicate upwelling (positive gradient) and blue tints indicate downwelling (negative gradient), at each 1° by 1° grid column. The two subplots below each panel show how two single particles behave in the vertical (left y-axis) throughout the latitudes during their lives (orange and magenta lines). The minimum and maximum sampled bathymetry along the particle trajectories are reprented by the black and grey areas, respectively. The green lines represent the sampled 20-years averaged potential density (σ_0) along the particle trajectories. . . . 68

List of Tables

2.1 For each sensitivity experiment to the parameters of the experimental set up (first column), we present the difference between the sensitivity and the control experiment in the percentage of particles reaching one of the Atlantic-Arctic gates out of the total number of particles injected in both configurations (second and third columns). The control experiment is run according to the experimental setup described in Section 2.2.1 for the year 186 exclusively (instead of year 181 to 200). 15

2.2 Ocean volume transport (OVT) and ocean heat transport (OHT) across the Barents Sea Opening and Fram Strait for waters flowing into the Arctic for each model configuration and observations. The Eulerian estimates (Eul.) for HighRes and MedRes are the 20-year averages of transport and their interannual variabilities, computed across the discretized gate lines following the model grid. The Lagrangian estimates (Lag.) of volume and heat transport are calculated respectively from the sum of eqs. 2.1 and 2.2 and across the gates and averaged within the time period defined by the white areas in Fig. 3.6. Details on the definition of the boundaries of this area are to be found in the same figure. Observations (Obs.) are from [1]Smedsrud et al., 2013, [2]Schauer et al., 2004, [3]Skagseth et al., 2008, and [4]Skagseth et al., 2011. 16

List of Abbreviations

- **AMOC**: **A**tlantic **M**eridional **O**verturning **C**irculation
- **AW**: **A**tlantic **W**aters
- **BSO**: **B**arents **S**ea **O**pening
- **EGC**: **E**ast **G**reenland **C**urrent
- **FS**: **F**ram **S**trait
- **GFDL**: **G**eophysical **F**luid **D**ynamics **L**aboratory
- **MOM5**: **M**odular **O**cean **M**odel **5**$^{\text{th}}$ version
- **NAC**: **N**orth **A**tlantic **Current**
- **NAO**: **N**orth **A**tlantic **O**scillation
- **OHT**: **O**cean **H**eat **T**ransport
- **OVT**: **O**cean **V**olume **T**ransport
- **WSC**: **W**est **S**pitsbergen **C**urrent

1. Introduction

The Arctic Ocean has been losing ice in all regions and during all seasons over the satellite record (Stroeve & Notz, 2018). The ice cover has become younger and thinner, and its areal extent has shrunk, leading to an increased probability of rapid ice-loss events during summer. In contrast to 1984, when 30% of the April sea ice cover was over 5 years old, merely 2% of the April sea ice consisted of ice of that age in 2018. Nowadays, the onset of melting occurs 12 days earlier than at the beginning of satellite record, while freeze-up occurs 28 days later (Stroeve & Notz, 2018). When the surface sea ice melts, its surface albedo is lowered, increasing the amount of the Sun's energy absorbed by the ice surface, ultimately leading to further ice melting. When the ice has completely melted, the increased solar radiation reaching the ocean surface is efficiently absorbed by water. This heat is released by the ocean later in the season leading to an increase in Arctic air temperatures in autumn and winter which ultimately results in later ice formation (Serreze et al., 2009). This positive feedback is one of the underlying mechanisms of Arctic amplification whereby northern high latitudes have been warming faster than the global mean during the last decades (Huang et al., 2017) and why the Arctic is particularly vulnerable to climate change (Timmermans & Marshall, 2020).

The decrease in Arctic sea ice has extensive impacts on the Earth system as a whole. The increased surface warming and lowered atmospheric pressures in the Arctic resulting from sea ice loss are known to weaken the westerlies and ultimately bring extreme temperatures to lower latitudes (Bhatt et al., 2014). Furthermore, in recent autumns, the Arctic Ocean has experienced warmer and fresher waters, leading to a rise in permafrost temperatures in the northernmost and coldest regions of the Arctic (Bhatt et al., 2014). Permafrost thawing impacts significantly atmospheric chemistry as terrestrial methane emissions are expected to increase, with the precise magnitude yet to be determined (Lannuzel et al., 2020). Reduced ice cover also adversely affects regional flora and fauna, particularly species that depend on sea ice, such as sea ice algae and big mammals like polar bears or walruses (Bhatt et al., 2014).

All of these environmental changes have socio-economical impacts on the ~ 4 million Arctic inhabitants (Ford et al., 2021). Near-surface permafrost projected to melt by the middle of the century hosts 48% to 87% of Arctic infrastructures such as pipelines, roads, and buildings (Hjort et al., 2018). It is also worth mentioning the attachments that Arctic Indigenous Peoples have to ancestral lands and to their habits, such as hunting or fishing (Ford et al., 2021). Finally, The extensive loss of sea ice has revealed more open water, extending the shipping season and opening new routes in the Arctic Ocean. Over the past decade, ship traffic in the Canadian Arctic region has nearly tripled (Dawson et al., 2018). This increased accessibility will also unlock fishing grounds that were previously inaccessible and enhance access to Arctic oil, natural gas, and mineral resources (O'Garra, 2017). These opportunities bear a high potential for disruption to regional ecosystems and for escalation of geopolitical tensions (O'Garra, 2017).

The Arctic sea ice melt observed over the satellite period is thought to be driven by a combination of changes occurring in the atmosphere and ocean which are amplified by strong climate feedbacks acting in the region (Goosse et al., 2018). While the precise attribution of these changes is still being determined, it is clear that anthropogenic forcing plays a significant role in the ongoing warming and sea ice melting observed in the Arctic (He et al., 2019). The warming of the Arctic Ocean plays a leading role in the shrinking and thinning of sea ice (Carmack et al., 2016; Polyakov et al., 2017). This warming is mainly caused by increased ocean heat transport (OHT) through the main Arctic gates in the Atlantic and Pacific sectors, with a predominant role played by the Atlantic-Arctic gates (Oldenburg et al., 2024; Tsubouchi et al., 2021).

In the Atlantic sector, heat enters the Arctic Ocean through two main gates: the Barents Sea Opening (BSO) and the Fram strait (FS). Annually and on average, 73 TW (Smedsrud et al., 2010) and 37 ± 5 TW (Smedsrud et al., 2013) of heat are transported through these gates, respectively. During the recent decade, both gates have seen an increase in OHT, with an increase of 3.29% over 1998-2016 for BSO (Docquier & Koenigk, 2021; Docquier et al., 2020), which has been directly linked to the sea ice loss observed in the Eurasian Basin (Ivanov et al., 2012; Onarheim et al., 2014; Polyakov et al., 2017). Models have shown rapid sea ice declines to be caused by pulses of ocean heat (Holland et al., 2006). These rapid declines occur primarily in winter over shallow continental shelves following the penetration of the relatively warm Atlantic Waters (AW) through BSO (Auclair & Tremblay, 2018). At FS, the large amount of heat carried by the AW enters at depth, hence reducing the impact of this heat on the sea ice (Dörr et al., 2024). Until the 2000s, a cold halocline layer typical of the Arctic Ocean was shielding the sea ice from the AW (Aagaard et al., 1981). This shield has, however, been weakening since due to the warming and increased penetration of AW into the Arctic basin, a process dubbed ”Atlantification” (Polyakov et al., 2017). The Atlantification is associated with a reduction in sea ice cover and stratification in the eastern Eurasian Basin (Polyakov et al., 2017).

AW originate from the Eastern North Atlantic where it acquires its warm and salty signature. To get to the Arctic Basin, AW first follow the North Atlantic Current (NAC) before joining the Nordic Seas (Fig. 1.1). Around 50°N, the NAC divides into three branches; from

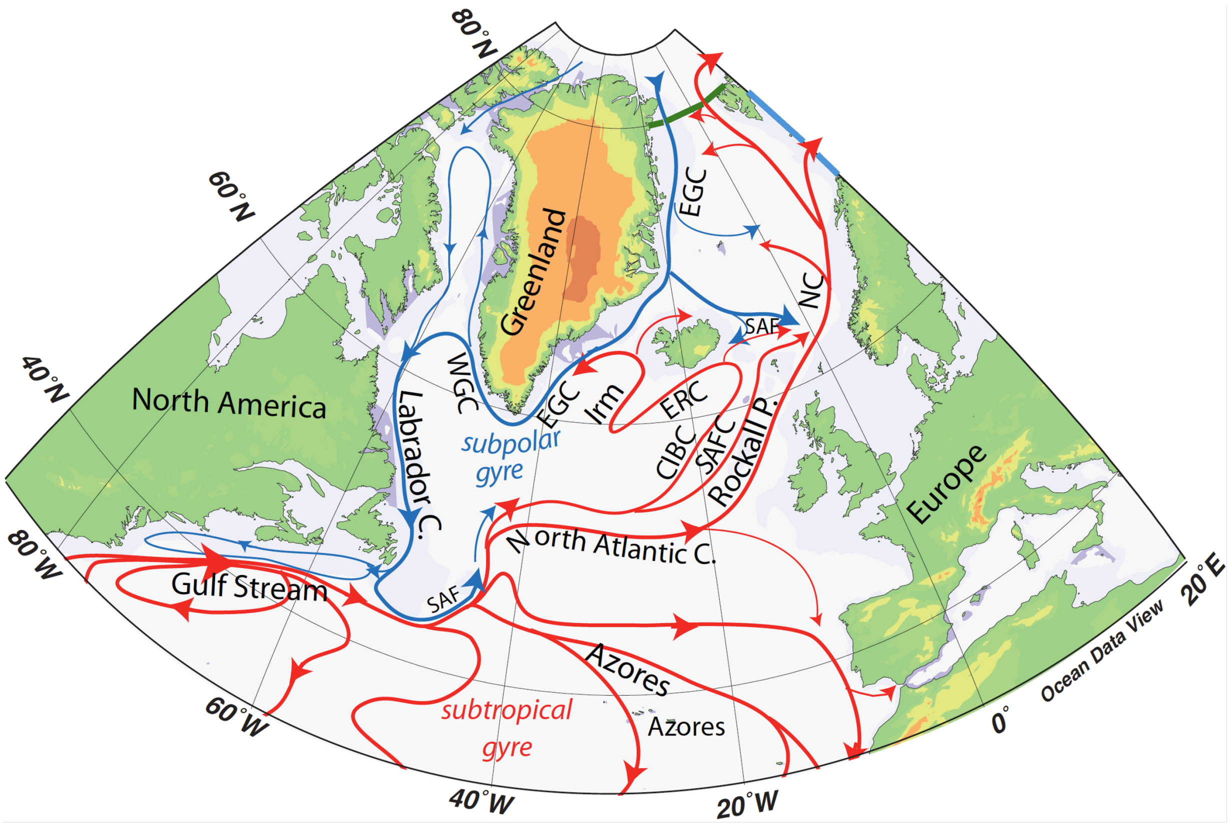

Figure 1.1: Schematic of the North Atlantic and Nordic-Sea circulations. The red arrows represent warm water currents, and the blues ones cold water currents. [Norwegian Current (NC), East Greenland Current (EGC), Subarctic Front Current (SAFC), Central Iceland Basin Current (CIBC), East Reykjanes Current (ERC), Irminger Current (Irm), West Greenland Current (WGC), Subarctic Front (SAF)]. The lightblue and darkgreen lines represent the Barents Sea Opening and the Fram Strait respectively. (Modified from Fig. 3-34 in Fieux, 2017).

east to west: the Rockall Passage Current, the Subarctic Front Current, and the Central Iceland Basin Current. As they approach Iceland, the Rockall Passage Current, the Subarctic Front Current, and a small portion of the Central Iceland Basin Current merge to form the Norwegian Current, while the remaining part of the Central Iceland Basin Current becomes the East Reykjanes Current. The East Reykjanes Current then splits west of Iceland, with a small branch flowing around Iceland to join the Norwegian Current, while the remaining branch forms the Irminger Current, later joining the East Greenland Current (EGC) flowing along Greenland's coast. Water in the EGC eventually cools and becomes trapped in the subpolar gyre, circulating around the gyre and rejoining the NAC. In the Nordic Seas, the

Norwegian Current follows the Norwegian coastline before splitting at about 70°N into the West Spitsbergen Current (WSC) that reaches FS and the North Cape current that enters the Barents Sea. Some AW recirculate along their journey to the Arctic gates with a fraction eventually joining the ECG when branching off to the west (Huang et al., 2021).

The greater ocean heat transfer to the Arctic observed in the last decades has been tied to an increase in volume transport and a rise in AW temperature, separately or in combination. Some studies suggest that the increase in heat transport is strongly controlled by ocean volume transport (OVT) rather than by increasing water temperature, both on short and long time scales (e.g., Madonna and Sandø, 2022; Muilwijk et al., 2018). However, Oldenburg et al. (2018) indicated that there is a certain interplay between both when changes are driven by internal (natural) variability or external (greenhouse gas-induced) forcing. When driven by internal variability, an enhanced Atlantic meridional overturning circulation (AMOC) is correlated with enhanced OHT, meaning that the OVT dominates. But when driven by external forcing, the AMOC weakens, yet an enhanced OHT is still observed, revealing that temperature dominates. In a future where global warming continues, changes in sea ice extent would thus likely be dominated by a weakening AMOC transporting warmer water (e.g., Nummelin et al., 2017; Sévellec and Fedorov, 2016).

The pathways followed by the AW towards the Atlantic-Arctic gates determine the distribution of heat between the Barents Sea and the deep Arctic basin with implications for the sea ice cover. These pathways are strongly steered by the bottom topography. In the North Atlantic and the Nordic Seas, the combination of a weak planetary vorticity gradient and a weak density stratification strengthens the role of bottom topography (Trodahl & Isachsen, 2018). The powerful topographic steering in these regions is the source of sharp fronts associated with high flow variability, prone to baroclinic and barotropic instabilities that generate mesoscale eddies (Trodahl & Isachsen, 2018). In the Atlantic Ocean, these eddies have been shown to have a key role in the circulation by driving the recirculation and subduction of AW entering the Arctic (Hattermann et al., 2016; Wekerle et al., 2020). The resolution of numerical models is thus expected to significantly impact the representation of heat transport towards the Arctic.

In coarse-resolution models, OHT into the Arctic is found to be generally largely underestimated compared to observations (Mahlstein & Knutti, 2011). Coupled Model Intercomparison Project Phase 6 models, with typical nominal resolution of 1°, show too deep and thick AW at FS, as well as inaccurate inflow and outflow structure across the gate, with implications for the stratification in the deep Arctic Basin (Heuzé et al., 2023). As the resolution of ocean models increases, North Atlantic currents are found to intensify and the circulation resembles more that observed (e.g., Docquier et al., 2019, 2020; Grist et al., 2018; Madonna & Sandø, 2022; Roberts et al., 2016). The pathways of AW into the Barents Sea is also shown to be better represented in finer resolution models (Docquier et al., 2020).

Yet, even though more heat is brought from the North Atlantic towards the Arctic as model resolution is refined, the distribution of this heat between the gates and the depth of penetration into the Arctic determines largely the fate of sea ice. Using two configurations of a climate model at different eddying resolutions, Decuypère et al. (2022) showed that while their finer resolution model had the largest northward heat transport in the North Atlantic, it had the lowest heat transport across the Atlantic-Arctic gates. These differences in OHT are presumably caused by differences in the pathways of AW towards the Arctic. The representation of bottom topography and ocean dynamic features, such as mesoscale eddies, are known to affect the position, strength and variability of currents. The rich scientific literature on the causes of Arctic sea ice decline in the Eurasian Basin highlights that the variability and intensity of ocean heat transport through the main Atlantic-Arctic gates remains a major source of uncertainty for predicting the future sea ice in this region

(Mahlstein & Knutti, 2011).

While a lot of the interest has been so far on quantifying the OHT and its variability across the Atlantic-Arctic gates and its impacts on the sea ice, we focus here on the pathways of AW towards the main Atlantic-Arctic gates with the hypothesis that a refined representation of bottom topography and ocean dynamic features might significantly impact the routes followed by AW. To do so, we use two versions of a climate model with different eddying horizontal resolutions and follow a Lagrangian approach to examine how the representation of seafloor topography and ocean currents influence the AW pathways and heat transferred into the Arctic in the two model configurations.

2. Methods

2.1 Model and Simulations

2.1.1 The CM2-O climate model suite

We use two configurations of the Geophysical Fluid Dynamics Laboratory (GFDL) CM2-O climate model suite (Delworth et al., 2012; Griffies et al., 2015) which solely differ in the horizontal resolution of their ocean component: the eddy-permitting CM2.5 (0.25°) and the eddy-rich CM2.6 (0.10°). For the sake of clarity, we henceforth refer to these two configurations as *MedRes* and *HighRes*, respectively.

The ocean model in both of the configurations is the fifth version of the Modular Ocean Model (MOM5; Griffies et al., 2015) with a vertical grid configuration of 50 cells distributed across the entire ocean column down to 5500 m. The vertical grid resolution is finer close to the surface (10 m) and coarser at depth (210 m). It uses $z^\star$ generalized vertical coordinates, allowing for time-dependent grid cell thicknesses as the free surface fluctuates. The model uses a tripolar grid (Murray, 1996), with one pole at the south pole and two additional ones placed over Northern Canada and Russia to avoid singularity at the North Pole. The ocean model uses the piecewise parabolic method, a third-order finite volume advection scheme (Delworth et al., 2012) and the K-profile parameterization scheme for vertical mixing

(Large et al., 1994). For both HighRes and MedRes, the model does not use any parameterization for representing the impact of mesoscale eddies on the circulation and mixing. To dissipate the downscale enstrophy cascade near the grid scale, a biharmonic friction operator is implemented in the momentum equation (Griffies & Hallberg, 2000). Both configurations use a parameterization for the effects of sub-mesoscale, mixed layer eddies (Fox-Kemper et al., 2011). The ocean model includes a simplified version of the prognostic biogeochemical model Biogeochemistry with Light Iron Nutrients and Gas (Galbraith et al., 2010) called miniBLING, which comprises three prognostic tracers: dissolved inorganic carbon, a dissolved inorganic macro-nutrient (called PO_4), and dissolved oxygen (O_2) (Galbraith et al., 2015). Despite its reduced complexity, miniBLING has been shown to be applicable to a range of problems and to be particularly useful to look into the transport of biogeochemical tracers by the physical circulation (Claret et al., 2018; Dufour et al., 2015; Frenger et al., 2018; Yamamoto et al., 2018).

The sea ice component is the GFDL Sea Ice Simulator, which consists of a modified Semtner thermodynamic three-layer scheme (one snow layer and two ice layers) and five ice thicknesses categories (Delworth et al., 2006; Semtner, 1976; Winton, 2000). Ice internal stresses are calculated from the elastic-viscous-plastic model of Hunke and Dukowicz (1997). The model uses the same tripolar grid as the ocean component, meaning that its resolution varies between the two configurations (Dunne et al., 2012). The iceberg model of Martin and Adcroft (2010) is included to represent the transport of land ice and subsequent melting away from land. The atmospheric component is the GFDL Atmospheric Model 2.1, with a horizontal resolution of 50 km and 32 vertical levels (Delworth et al., 2012). The model is constructed on a "cubed-sphere" grid with the advective terms computed from a modified Euler backward scheme (Kurihara & Tripoli, 1976). Finally, the land component is the Land Model 3 with flow pathways from Milly et al. (2014). A more detailed and complete description of each component of the CM2-O model suite can be found in Delworth et al.

(2012) and Griffies et al. (2015).

2.1.2 Preindustrial simulations

Both HighRes and MedRes configurations are run for 200 years from an initial state provided by the World Ocean Atlas 2009 (Antonov et al., 2010; Garcia et al., 2010; Locarnini et al., 2010) under a preindustrial control scenario using a constant and globally averaged atmospheric Carbon dioxide (CO_2) concentration set at 286 ppmv, mirroring levels from 1860. The preindustrial simulation was chosen over its climate change counterpart to assess the climate in an undisturbed state. This avoids the complications of potentially different responses to anthropogenic forcing in the two configurations and allows for a focus on comparing the change in resolution. Only one ensemble member was run for each configuration due to the high computational and storage cost of HighRes. Important circulation features as the upper cell of the Atlantic meridional overturning circulation (AMOC), the Antarctic Circumpolar Current, and global sea surface temperature reach near equilibirum after 100 years (Dufour et al., 2015; Fortin et al., 2023).

These preindustrial control simulations, as well as their climate change simulation counterparts, have been documented in many papers. It was found that HighRes accurately represents key elements of the northwest Atlantic circulation, eliminating a warm and salty bias on the Scotian shelf and ultimately allowing for a more realistic Gulf Stream compared to coarser resolutions models (Caesar et al., 2018; Claret et al., 2018; Saba et al., 2016). Furthermore, Griffies et al. (2015) noticed a southward shift of the North Atlantic Current (NAC) relative to observations both in HighRes and MedRes due to the instability of the Gulf Stream closer to the coast, with the smallest bias found in HighRes (Saba et al., 2016). This bias has been linked to an inaccurate representation of Northern overflows, notably in the Nordic Sea where the deep water contributes to the deep branch of the AMOC (Saba

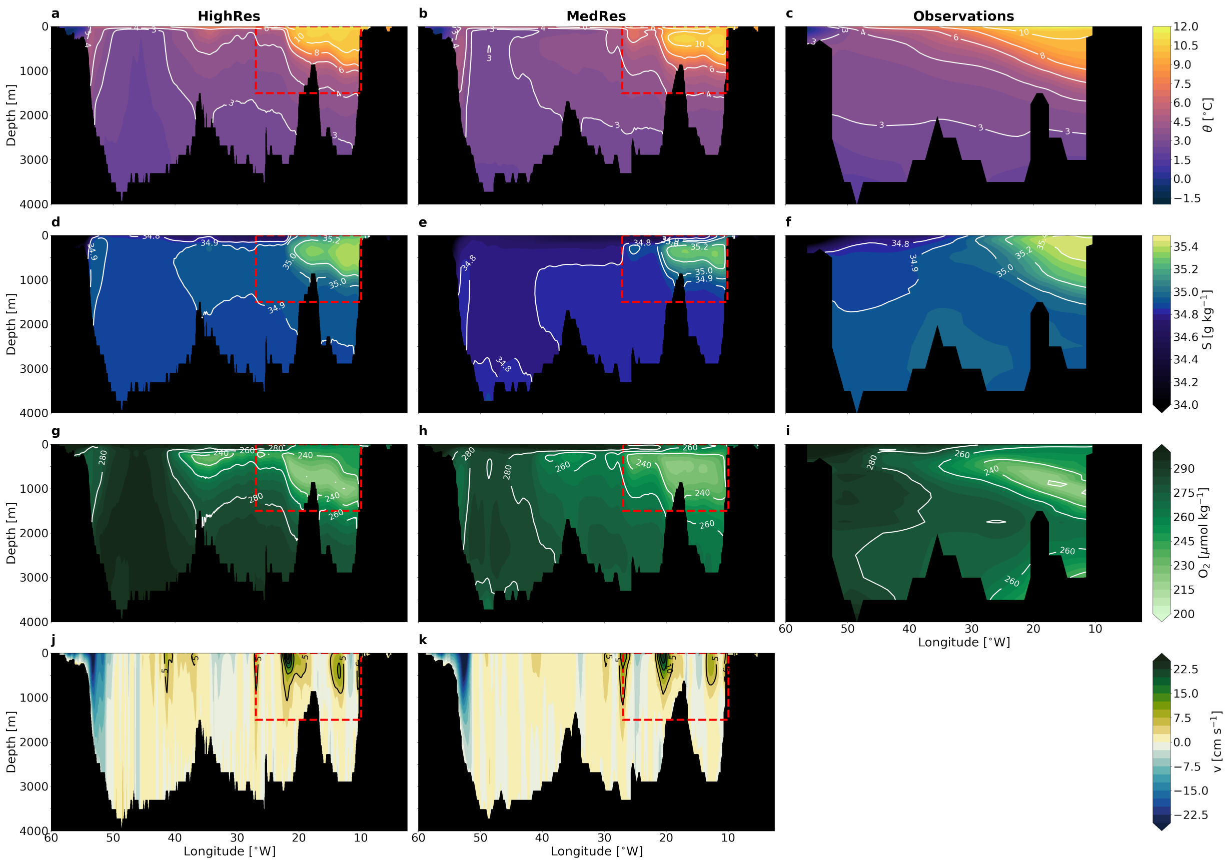

Figure 2.1: 20-year averaged (a-c) potential temperature (θ), (d-f) salinity (S),(g-i) oxygen concentration (O_2), and (j-k) meridional velocity (v), and their respective isocontours (white/black contours) along 55°N, in the two model configurations and the observations. The observational fields are from the World Ocean Atlas 2009 (Antonov et al., 2010; Garcia et al., 2010; Locarnini et al., 2010). In the first two columns, the dashed red box delineates the initialization zone of virtual particles. The bathymetry in the last row is different as the velocities are located on the northeast corner of the gridcells, and not in the center of the gridcells as for the tracers.

et al., 2016).

Compared to observations, HighRes and MedRes represent generally well the pattern and magnitude of the main water properties in the North Atlantic along 55°N (Fig. 2.1). Both resolutions capture the northward-flowing warm, salty, and poorly oxygenated Atlantic Waters (AW) on the eastern side of the transect. Observational data show temperatures decreasing more gradually to the west compared to the models, which display a sharper transition to

the subpolar gyre water, characterized by steep isotherms from 20°W onwards. Salinity and O_2 fields show similar patterns, with salinity being underestimated in both configurations, especially in MedRes. The poorly oxygenated water west of the minimum extends slightly further westward in both configurations compared to observations, with a second area with a O_2 concentration around 240 mmol kg^{-1} at 35°W in HighRes, which is less discernible and more oxygenated in MedRes. This secondary branch of the AW (Daniault et al., 2016) is weakly visible in the temperature and salinity fields, with the slight westward extension of salty and poorly oxygenated water better represented in HighRes than in MedRes. Additionally, a cold, fresh, and oxygenated cap is present above the AW from approximately 25° to 10°W. This feature, which does not appear in the observations, is likely formed in the western part of the basin and carried eastward by the subpolar gyre. Both configurations show clear signs of deep convection in the Labrador Sea that explains most of the biases in temperature, salinity and O_2 in the western side of the section throughout the water column. Most climate models overestimate deep convection in the Labrador Sea with consequences for the AMOC (Heuzé, 2017). One should keep in mind though that both configurations used here are run under a preindustrial scenario which limits the extent of the comparison with observations made.
Three northward flowing branches are visible along the initialization transect (Fig. 2.1j-k). These most probably correspond to CIB, the Subarctic Front Current and the Rockall Passage Current represented in (Fig. 1.1). In both configurations, the Subarctic Front Current branch seems to be the strongest one. The Subarctic Front Current and the Rockall Passage Current seem to extend as bit more throughout the latitudes and depths in HighRes, while this is the case for the Central Iceland Basin Current in MedRes. Overall, they are horizontally centered around the same latitudes throughout the configurations.

The meridional net heat transport at 56°N is found to be 0.49 ± 0.03 and 0.43 ± 0.02 PW in HighRes and MedRes, respectively, which compares relatively well to the observational estimate of 0.37 ± 0.07 by Holliday et al. (2018). The slight overestimation of HighRes is very typical of climate models of the same generation (Docquier et al., 2019; Grist et al., 2018).

2.2 Lagrangian tracking experiments

2.2.1 Experimental set up

For each model configuration, we perform an offline Lagrangian forward-tracking experiment with Parcels version 3.0.2 (Delandmeter & van Sebille, 2019; Lange & van Sebille, 2017). Virtual passive particles are initialized in the North East Atlantic at 55°N, within the warm and saline water carried by the NAC towards the Arctic, which are often referred to as the AW as they enter the Nordic and Greenland Seas (Fig. 2.2). To do so, the initialization domain is chosen to delimit regions exhibiting pronounced signals in potential temperature

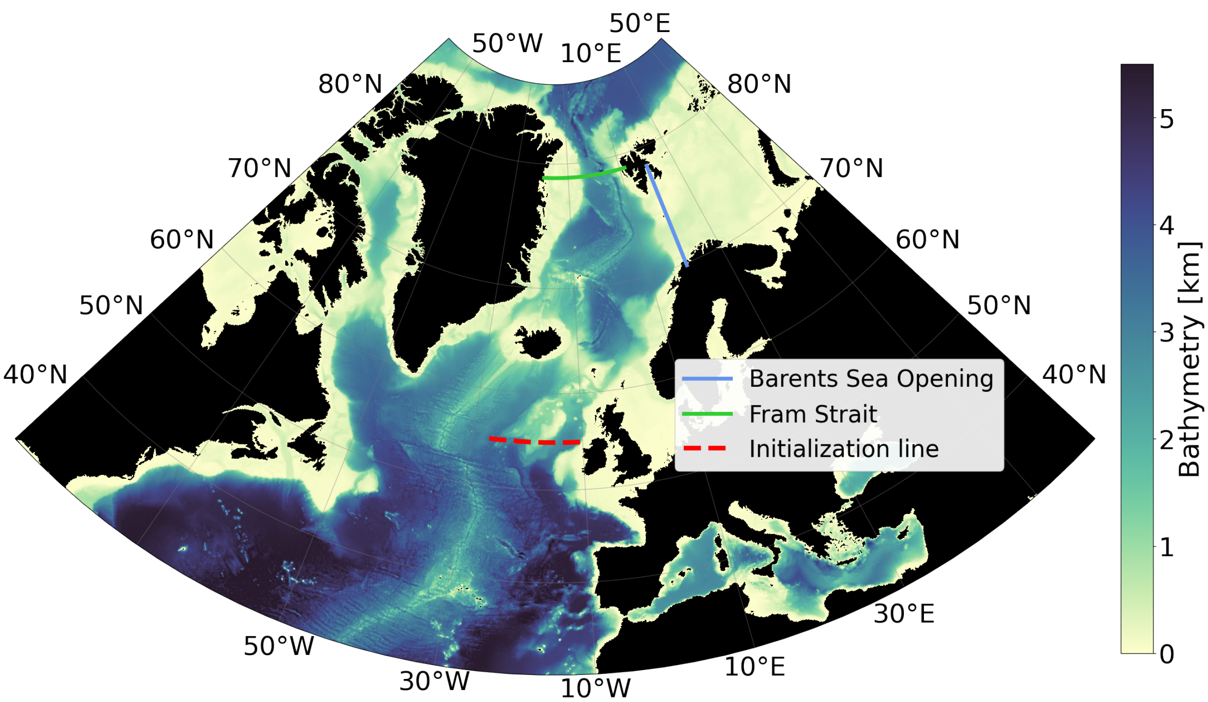

Figure 2.2: Bathymetry of the HighRes configuration, with the location of the two gates of interest and of the line where particles are initialized before being advected.

and salinity along 55°N and to include the three main branches of the NAC (Fig. 2.1). These relatively warm ($\geq$ 5°C) and salty ($\geq$ 35 g kg^{-1}) waters are found down to ~1500 m in the eastern part of the 55°N section within the main northward flowing branches of the NAC as shown in Fig. 2.1. We choose to extend the domain to encompass the three main branches of the NAC (Fig. 2.1i-k). The northward branch sitting on the western side of the mid-Atlantic ridge is left out of the domain as it presumably does not feed the Nordic Seas. The injection of the particles is done every 0.05° horizontally and every 10 m vertically within the limits of the injection box shown in Fig. 2.1 and is repeated every week for 10 years. After having drifted in the domain for 10 years, particles are killed. Overall, a total of 26.0 10^6 and 26.3 10^6 particles are injected in HighRes and MedRes, respectively.

From their initialization point, the particles are allowed to go both northward and southward, and are advected using a 4$^{\text{th}}$ order Runge-Kutta scheme by the 5-day averaged 3-D velocity fields. Particle positions are calculated every 6 hours and written every 5 days. Our implementation includes the correction of a bug that did not take into account the rotation of velocity vectors in the MOM5 Arctic bipolar grid (`from_mom5()` advection method in Parcels). Details regarding the implemented fix can be found in Appendix A. Particles reaching the domain's horizontal boundaries (from 30°N to 90°N, and from 100°W to 80°E) or hitting the ocean bottom during their lifetime are killed, while those escaping the ocean surface are pushed back to it. The experiment is carried out over the last 20 years of the preindustrial control simulations as 5-day averaged velocity fields were only saved over that period, the monthly averages otherwise available over the 200 years being of too low frequency to provide a good representation of the total velocity field (van Sebille et al., 2018). No diffusion scheme is used as no consensus exists on how to include diffusion and mixing in Lagrangian tracking experiments (van Sebille et al., 2018). The Eulerian velocity fields should, however, reflect these processes through their effects on the modelled tracer field. Moreover, Tamsitt et al. (2017) showed that the Lagrangian trajectories and associated

	HighRes	MedRes
Init. every 5 days	$3.72\,10^{-3}$	$3.13\,10^{-2}$
0.1° horiz. spacing	$-3.27\,10^{-2}$	$-9.71\,10^{-3}$
2-hr calculation timestep	$1.27\,10^{-2}$	$2.69\,10^{-2}$
12-hr calculation timestep	-0.15	$-2.02\,10^{-3}$
Barents Sea Opening 1°W	$2.56\,10^{-2}$	$2.76\,10^{-2}$
Barents Sea Opening 1°E	$-2.26\,10^{-2}$	$-2.70\,10^{-2}$
Fram Strait 1°S	1.05	0.87
Fram Strait 1°N	-1.41	-0.18

Table 2.1: For each sensitivity experiment to the parameters of the experimental set up (first column), we present the difference between the sensitivity and the control experiment in the percentage of particles reaching one of the Atlantic-Arctic gates out of the total number of particles injected in both configurations (second and third columns). The control experiment is run according to the experimental setup described in Section 2.2.1 for the year 186 exclusively (instead of year 181 to 200).

transports were relatively insensitive to the inclusion of such schemes in the Southern Ocean in HighRes. To investigate the trajectories of AW on their way to the Arctic, particles are tagged each time they cross the Barents Sea Opening (BSO) or the Fram Strait (FS). If a particle crosses both BSO and FS during its lifetime, it is tagged based on the gate it crossed first. The sections used to delimit the two Atlantic-Arctic gates are placed in order to follow a constant longitude for BSO (20°E) and a constant latitude for FS (79°N) (Fig. 2.2).

To assess the robustness of the experimental set up, a sensitivity analysis is conducted which involves varying key parameters to observe their effects on the number of particles reaching the gates (Table 2.1). Overall, altering key parameters does not significantly affect the percentage of particles reaching the gates with changes remaining within 10^{-2}% except for two cases. The first case occurs when the calculation time step is extended to 12 hours instead of 6 hours. Calculating the particle positions every 12 hours instead of 6 hours results in fewer particles reaching the gates, especially for HighRes, with a decrease of about 0.15%. In contrast, increasing the time step to 2 hours offers minimal benefit, as it only increases the number of particles reaching the gates by an order of magnitude of 10^{-2}% in both configurations. We thus settle on 6 hours for the advection time step. The second case relates to the position of the section delineating FS. Shifting the section from 79°N to 78°N

		Barents Sea Opening			Fram Strait		
		Lag.	Eul.	Obs.	Lag.	Eul.	Obs.
HighRes	OVT [Sv]	0.58	2.58 ± 0.25	3.2[1]	0.70	4.93 ± 1.16	9 ± 2[2]
	OHT [TW]	10.5	43.0 ± 6.34	82[3,4]	7.47	43.2 ± 10.2	28 ± 5 to 46 ± 5[2]
MedRes	OVT [Sv]	0.66	2.99 ± 0.28	3.2[1]	0.36	3.10 ± 0.46	9 ± 2[2]
	OHT [TW]	11.1	51.0 ± 9.00	82[3,4]	2.98	34.9 ± 4.05	28 ± 5 to 46 ± 5[2]

Table 2.2: Ocean volume transport (OVT) and ocean heat transport (OHT) across the Barents Sea Opening and Fram Strait for waters flowing into the Arctic for each model configuration and observations. The Eulerian estimates (Eul.) for HighRes and MedRes are the 20-year averages of transport and their interannual variabilities, computed across the discretized gate lines following the model grid. The Lagrangian estimates (Lag.) of volume and heat transport are calculated respectively from the sum of eqs. 2.1 and 2.2 and across the gates and averaged within the time period defined by the white areas in Fig. 3.6. Details on the definition of the boundaries of this area are to be found in the same figure. Observations (Obs.) are from [1]Smedsrud et al., 2013, [2]Schauer et al., 2004, [3]Skagseth et al., 2008, and [4]Skagseth et al., 2011.

increases the percentage of particles reaching the gates by 1.05% and 0.87%, while shifting it to 80°N decreases the percentage by 1.41% and 0.18% in HighRes and MedRes, respectively. These differences can be attributed to the two recirculating branches of the Return Atlantic Water detaching from the West Spitsbergen Current (WSC) and joining the East Greenland Current (EGC) rather than penetrating into the Arctic Basin (Fig. 1.1). While one branch is located around 78°N, the other is located slightly further north at approximately 79°N (Wekerle et al., 2020). When the section is shifted north, the percentage decreases as many particles recirculate before reaching the gate. Conversely, when shifted south, particles are flagged as having crossed FS even if they recirculate downstream. Positioning the FS at 79°N ensures a focus on particles penetrating into the Arctic Basin while also capturing some of the recirculation in the area.

The Eulerian estimates for volume and heat transports of waters flowing into the Arctic through those gates are compared to observations in both configurations in Table 2.2. At BSO, HighRes underestimates the eastward volume transport by ∼10-20% while MedRes shows a good match with observations. At FS, both configurations largely underestimate the northward volume transport by at least 50%. The negative bias in volume transport combined with that in the modeled temperatures due to the use of a preindustrial scenario lead to a strong negative bias in heat transport at BSO in both configurations. In particular, the AW heat transport into BSO and FS has been very high over the past decade (Årthun & Schrum, 2010; Schauer et al., 2008). This bias persists in HighRes while it disappears in MedRes under a climate change scenario (see Table 1 for net heat transport in Decuypère et al., 2022, "Medium" corresponds to our MedRes while "High" corresponds to our HighRes). Interestingly, at FS, the modeled heat transport falls within the range of uncertainties from observations.

2.2.2 Computation of volume and heat transport

To compute the volume and heat transported by the AW in our Lagrangian experiments, we assign a volume to each particle at initialization. To do so, each particle is attributed an area at its starting position, defined by multiplying the horizontal spacing between the particles, $dx = 0.05°$, by the vertical spacing between them, $dz = 10$ m (Appendix B). For particles seeded at the surface, we take $dz = 5$ m instead, which is half the distance between the surface and the next row of seeded particles at depth. The dz value remains constant regardless of whether particles initialized at the surface drift at depth, and vice versa. By taking the meridional velocity, v^P, of a given particle P interpolated by Parcels in the center of the area at initialization, we can compute the volume transport associated to that particle which we assume to remain constant throughout the life of the particle:

$$V^P_{trans} = dx\, dz\, v^P \tag{2.1}$$

Tagging the particles with a constant volume is a valid approach when working with a model run with volume-conserving Boussinesq kinematics (see van Sebille et al., 2018, for a useful discussion on the limits of this approach), and has widely been used before (Lique et al., 2010; Tamsitt et al., 2017; Tooth et al., 2023; van Sebille et al., 2014). Heat transport can then be calculated for each particle P at any location and time of the experiment:

$$H^P_{trans}(t, x, y, z) = V^P_{trans}\, \theta^P(t, x, y, z)\, c_p\, \rho_0 \tag{2.2}$$

where θ^P is the potential temperature of the particle at a given location and time, $c_p = 3992.1$ J kg^{-1} K^{-1} the ocean heat capacity, and $\rho_0 = 1035$ kg m^{-3} the constant Boussinesq reference density. Potential temperature, as well as salinity and O_2 concentration, are calculated along the particle trajectories from an interpolation of the 5-day averaged potential temperature, salinity, and O_2 concentration fields of the run. Tracking these variables along the particle trajectories allow to assess the changes in the properties of the particles during their lifetime.

3. Results

3.1 Main and secondary pathways of Atlantic Waters from 55°N to the Arctic gates

From all the particles initialized, 6.90% and 7.08% reached either the Barents Sea Opening (BSO) or the Fram Strait (FS) in HighRes and MedRes respectively. The rest of them mainly recirculates within the subpolar gyre without reaching any gates during their lifetimes (not shown). These values represent 11.2% and 12.0% of the total volume transport initialized in HighRes and MedRes. In terms of volume transport crossing the Atlantic-Arctic gates, this corresponds to 1.28 Sv (HighRes) and 1.02 Sv (MedRes) on average.

The particle trajectories reveal the main pathways towards the Atlantic-Arctic gates and their relative importance (Fig. 3.1). In both resolutions, the main currents depicted in Fig. 1.1 account for more than 10% of the total particle transport that reaches the gates. Upon their initialization at 55°N, the particles follow one of the three main branches of the North Atlantic Current (NAC) which are the Rockall Passage Current, the Subarctic Front Current, and the Central Iceland Basin Current. The majority of the particles in the Rockall Passage Current and the Subarctic Front Current, as well as a branch East of Iceland detaching from the East Reykjanes Current, join the Norwegian Current subsequently. It is

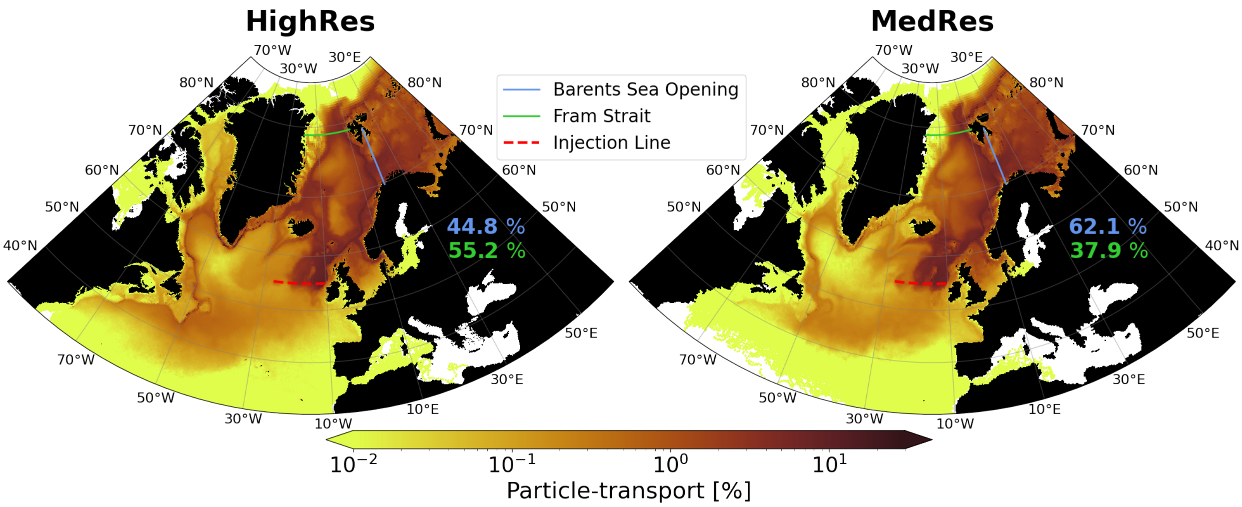

Figure 3.1: Main pathways towards the Atlantic-Arctic gates and relative importance of gates. Colors indicate the fraction of the total particle transport across the Atlantic-Arctic gates (Barents Sea Opening and Fram Strait) at each 0.25° by 0.25° grid column over the whole experiment. Grid cells with high values correspond to columns which have been visited either by many particles or by relatively fewer particles that are associated with high transport. Numbers overlaid on the continent correspond to the preference of particles entering the Arctic to go through Fram Strait or Barents Sea Opening first, expressed in particle-transport and color-coded by gate.

also worth noting that particles follow the northward branch West of Iceland detaching from the Irminger Current and flowing North of Iceland, making all the North-Atlantic northward warm branches from Fig. 1.1 discernable by more than 5% of the total particle-transport reaching both gates. On their way to the Arctic along the Barents Sea shelf, some of the particles recirculate in the Norwegian Sea around 65°N, as well as in the Greenland Sea at FS around 79°N before reaching BSO or FS. The recirculation branch in the Greenland Sea around 75°N visible in Fig. 1.1 is not discernible in Fig. 3.1, as particles having followed this branch most likely never reach one of the gates. After having crossed BSO, most particles drift in the Barents Sea before joining the Arctic boundary current through the St. Anna Trough or the Franz-Victoria Trough. After having crossed FS, particles follows the Yermak branch and Svalbard branch, continuing along the western slope of the Yermak Plateau and along the Svalbard shelf break, respectively. Particles ultimately join the Arctic boundary current, meeting those originating from the Barents Sea.

Beyond gates, some of the particles recirculate, carrying in total about 75.7% and 65.3% of the total particle-transport reaching the Atlantic-Arctic gates in HighRes and MedRes respectively. At BSO, entering particles either recirculate at the gate itself or exit slightly later between Bear Island and Svalbard, after having drifted on the Barents shelf. At FS, the majority of recirculating particles ($5-10\%$ particle-transport) are associated to the Return Atlantic Water which flows along a southwestward branch that detaches from the West Spitsbergen Current (WSC) and later joins the southward East Greenland Current (EGC) towards the subpolar gyre. Along the East and West Greenland Currents, a small portion of the particles ($0.1-1\%$ particle-transport) detach to visit Baffin Bay. Particles recirculating within the Baffin Bay then join the subpolar gyre again and flow southward along the Labrador Current until the Grand Banks where some of them join the NAC to flow back north again.

Though the main pathways appear similar at first-order in the two model configurations, substantial differences exist. A notable difference between the two model configurations lie in the circulation fork occurring at 60°N. In HighRes, particles display a stronger preference for following the Irminger Current than in MedRes. Of the particle-transport reaching the Atlantic-Arctic gates, 8.15% follow the Irminger Current in HighRes, compared to 6.17% in MedRes. This difference is even more pronounced for the particle-transport associated with the small branch that detaches from the Irminger Current and flows north of Iceland towards the Norwegian Current. This branch constitutes approximately 74.4% of the Irminger Current particle transport in HighRes, compared to 9.28% in MedRes. This indicates that while the majority of particles eventually reach the gates through the three currents detaching from the NAC in both configurations, there is also a secondary, weaker pathway that goes around Iceland before joining the Norwegian Current, this pathway being significantly stronger in

HighRes than in MedRes. More particle-transport is also found around the Iceland Plateau in HighRes than in MedRes. In HighRes, the small branch transporting warm water North of Iceland, ultimately joining the Norwegian Current (Fig. 1.1), has a corresponding particle-transport 13 times larger than in MedRes. This is most likely due to the higher tendency of particles to flow in the Irminger Current in HighRes than in MedRes, but it might also come from the eastward jets North of Iceland, better developped in HighRes than in MedRes. Indeed, jets just North of Iceland are stronger and eastwards until 68°N in HighRes, whereas these are almost absent or even westward in MedRes (not shown). Rather than joining the Norwegian Current as it does in HighRes, the current north of Iceland continues to go around Iceland and is prone to join the subpolar gyre again in MedRes (Appendix F). This actually happens but is not visible in Fig. 3.1, as the particles following this pathway do not reach the gates during their lifetime (not shown). The 0.25° resolution used in our MedRes make currents less turbulent than in HighRes which might make it more difficult for particles to detach from the main currents flowing around Iceland.

The transport partitioning between both Atlantic-Arctic gates exhibits a notable contrast between the two model configurations. While in HighRes, the transport across the Atlantic-Arctic is relatively well distributed between BSO (44.8%) and FS (55.2%), in MedRes, the bulk of transport across the Atlantic-Arctic gates occurs through BSO (62.2%; Fig. 3.1). In HighRes, particles tend to stay within the WSC while they branch off towards the Barents Sea at North Cape in MedRes. In HighRes, the Norwegian Current is significantly more confined to the coastline compared to MedRes, where it appears narrower and weaker throughout the top 500 m of the water column (Appendix F). Additionally, the branch of the Norwegian Current that detaches from the coastline and penetrates into the Barents Sea is stronger and extends across a broader range of latitudes in the top 100 m in MedRes. Consequently, particles tend to penetrate the Arctic more easily through BSO in MedRes than in HighRes, explaining the difference in particle-transport contributions per gate when the resolution is refined (Fig. 3.1).

In Highres more particles recirculate at FS compared to MedRes and subsequently follow the EGC before joining the subpolar gyre. The recirculation at FS is considerably stronger in HighRes, whereas in MedRes, the recirculation loop is barely visible (Appendix F). This outer branch has been reported to contain eddies controlling the amount of Atlantic Waters (AW) recirculation at FS, both in observational studies (Schauer et al., 2004; von Appen et al., 2016), as well as in model simulations (Hattermann et al., 2016; Wekerle et al., 2017). The recirculating branch shedding from the WSC might be weaker in MedRes due to a weaker and less well resolved eddy field, resulting in less particles recirculating into the EGC ($< 1\%$ particle-transport in MedRes versus $> 10\%$ in HighRes). There are more particles around the subpolar gyre in Highres than in MedRes ($1 - 10\%$ versus $0.1 - 1\%$ particle-transport). This might be attributed to a larger particle-transport in the Irminger Current as previously mentioned, and to the increased recirculation at FS into the EGC. More particles are also found in the center of the subpolar gyre in HighRes, while in MedRes, particles tend to stay within the boundary currents. As resolution is refined, eddy generation and transport is enhanced allowing for more waters, and hence particles, to leak towards the center of the subpolar gyre. Irminger rings and boundary current eddies have been reported to form from instabilities that develop within boundary currents due to steep topography and seasonal isopycnal slopes, respectively (Chanut et al., 2008).

Compared to MedRes, more particles visit Baffin Bay in HighRes ($0.01 - 0.1\%$ versus $0.1 - 1\%$ particle-transport). For the particles flowing in the subpolar gyre, 17.7% and 7.90% of the particle-transport reaching gates flow westward at the southern tip of Greenland in HighRes and MedRes, respectively. From this transport, 18.5% enters the Baffin Bay in HighRes, while only 9.59% does so in MedRes, showing that particles can more easily penetrate into Baffin Bay in HighRes than in MedRes. This increased penetration is due not only to more particles following the EGC and the West Greenland Current but also to stronger circulation there. In particular, the current along the west coast of Greenland in the Baffin Bay is stronger in the top 250 m in HighRes (Appendix F). As a consequence, there is a high temperature anomaly in this region in HighRes, as also noted by Decuypère et al. (2022), who used the same model configurations as us.

3.2 Inflow of Atlantic Waters at the Atlantic-Arctic gates

3.2.1 Barents Sea Opening

At BSO, the bulk of the particle-transport predominantly occurs at the southern edge between 70° and 73.5°N and throughout the water column in both configurations (Fig. 3.2a-b). Within this latitudinal range, two main entry points appear: a relatively high particle-transport between 70 and 72°N, and another, though weaker, particle-transport between 72 and 73.5°N. From 70 to 71°N, the southern branch consists of warm (> 4°C) and relatively fresh (< 34.6 g kg^{-1}) water along the coast, and as warm but saltier (> 34.6 g kg^{-1}) water away from the coast in both configurations (not shown). From 72 to 73.5°N, The northern branch consists of colder (> 2°C) and saltier water (> 34.6 g kg^{-1}; not shown). The fresh portion of the southern branch presents the characteristics of the Norwegian Coastal Current, transporting fresher water mixed with river inputs to create low-salinity shelf water (Rudels et al., 2004). The remaining saltier water present in both branches corresponds to the Norwegian Atlantic Slope Current, splitting in two branches at 72° and 73.5°N when reaching BSO (Skagseth et al., 2008).

In HighRes, there is a slight high salinity bias at the gate, which leads to a less distinct transition between the Norwegian Coastal Current and the Norwegian Atlantic Slope Current. In MedRes, the particle-transport is relatively weak between 70 and 71°N, except at the surface, while it remains relatively strong throughout the water column in Highres. Between these two latitudes, cross-sections of zonal velocities at the gate show shallower as well as weaker (0.5 cm s^{-1} versus > 1 cm s^{-1}) jets in MedRes than in HighRes (Appendix C). The splitting of the Norwegian Atlantic Slope Current at 72° and 73.5°N match well with the relatively high particle-transport visible at these latitudes. The two branches are particularly evident in MedRes, with the northern branch associated with a relatively higher particle-transport than in HighRes. The weaker incoming transport at that location

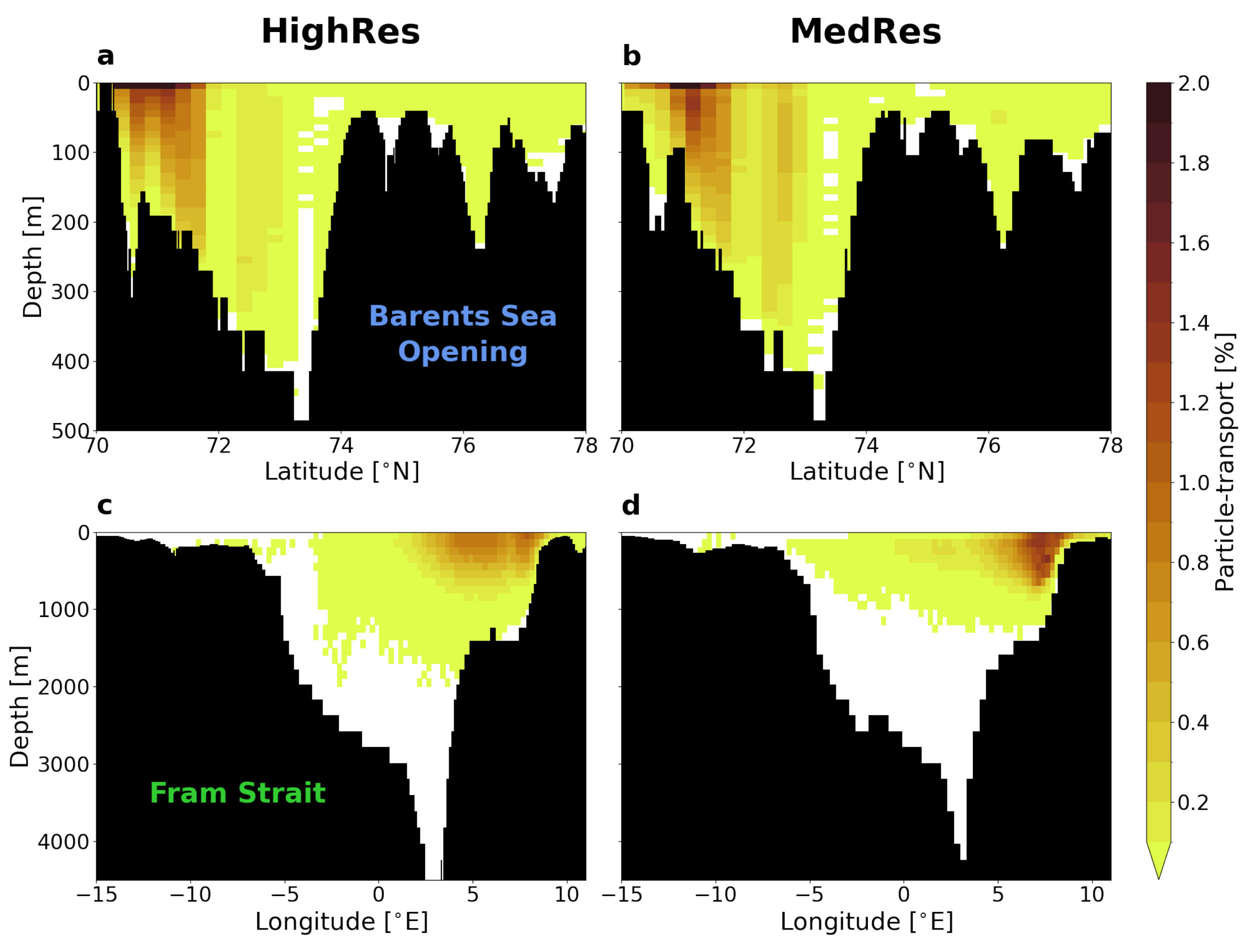

Figure 3.2: Vertical distribution of entering particle-transport at (a-b) Barents Sea Opening and (c-d) Fram Strait in both configurations. For each gate, colors indicate the fraction of particle-transport across that gate over the whole experiment. Particle-transport is binned into bins of 0.25° by 10 m for Barents Sea Opening, and 0.25° by 100 m for Fram Strait. Grid cells with high values have been visited either by many particles or by relatively fewer particles that are associated with high transport.

in HighRes is reflected in the temperature signal that shows waters about 2°C lower than in MedRes throughout the water column (not shown).

North of 73.5°N, fewer particles cross BSO and thus small particle-transport is found in both configurations, as expected from the circulation in this area (Appendix C). In particular, the passage north of Bear Island (74°N) is known to be an outflow route from the Barents Sea (Skagseth et al., 2008). Yet, recirculation occurs across the whole gate and through most of the water column in both configurations (Appendix D), explaining the small positive particle-transport found in this area (Fig. 3.2a-b). The strongest outflowing particle-transport occurs in the Bear Island Trough, just South of Bear Island (73.75°N; Appendix D), through the whole water column, consistent with the velocity field (Appendix C). The southern tip of Bear Island is known to be one of the main exit routes for the Arctic waters from the Barents Sea (Årthun et al., 2011). Atlantic water entering through the BSO recirculate within dense water formation areas in the Barents Sea as well as North of Bear Island (Skagseth, 2008), before joining the Norwegian Sea again through the BSO. These recirculation routes are well visible in both configurations, even though recirculation in the Bear Island Trough is stronger and extending more throughout latitudes in HighRes than in MedRes, and inversely for the recirculation North of Bear Island. These recirculation patterns are supported by the westward zonal velocities in the Bear Island region, with a stronger and deeper-reaching jet over most of the trough in HighRes, and surface-intensified velocities in MedRes (Appendix C).

3.2.2 Fram Strait

At FS, particle-transport primarily concentrates at the eastern edge and extends down to roughly 1 km in both model configurations (Fig. 3.2c-d). This strong particle-transport most likely corresponds to the WSC (Wekerle et al., 2020), reaching FS just west of Svalbard. Observations show that the core of the WSC is located on the eastern edge of the FS until around 8°E, characterized by a strong positive meridional velocity (> 15 cm s^{-1}) above 700 m, and relatively warm waters (> 1°C) (Beszczynska-Möller et al., 2012; Schauer et al., 2004). This branch seems to be well represented in both configurations, with the strongest northward jet across the gate present along the eastern edge of FS (Appendix C). Nevertheless, this branch is strongly underestimated with the meridional velocity in the core of the WSC not exceeding 5 cm s^{-1} and 4 cm s^{-1} in HighRes and MedRes respectively, where observations show velocities reaching up to 20 cm s^{-1} (Beszczynska-Möller et al., 2012). West of the current core and until around 5°E, which marks the shelf break, lies the offshore branch of the WSC, characterized by meridional velocities up to 15 cm s^{-1} extending until the seafloor (~ 2.6 km; Beszczynska-Möller et al., 2012). In HighRes, the boundary between the core and offshore branch of the WSC is clearly visible in the particle-transport, in contrast to MedRes. In both configurations, the particle-transport matches well the overall latitudinal and depth extent of the WSC coinciding with the positive temperature area (Beszczynska-Möller et al., 2012) in HighRes and MedRes (not shown).

In HighRes, some particles enter FS as deep as 2 km, while almost no particle reach below 1.2 km in MedRes (Fig. 3.2c-d). In the horizontal, the bulk of the particle transport extends to ~ 3°E in HighRes while it extends as far as 1°W in MedRes in agreement with the structure of the WSC in each model configuration. In HighRes, jets stronger than 1 cm s^{-1} extend down to 2 km, while they only reach 1 km depth in MedRes. Modelling studies have shown that as the horizontal resolution is refined, the representation of boundary currents improve (e.g., Chassignet et al., 2020) with narrower, stronger and deeper reaching jets. On the horizontal, a weak jet (> 1 cm s^{-1}) is present between 0° and 2.5°E just beneath the surface in MedRes, while absent in HighRes. This westward extension might partly explain the particle-transport west of 0°E in MedRes. It is also worth noting that non-zero particle-transport is found near the surface on the western side of the FS extending as far as the shelf in both configurations. At 12°W, a tiny but strong (> 4 cm s^{-1}) jet is found in HighRes, with a weaker expression in MedRes. This current carries less than 0.1% of the total northward particle-transport at the FS, however, consistent with the fact that the western part of the FS is mainly defined as an outflow route for Arctic water (Beszczynska-Möller et al., 2012).

Passed FS, a significant number of particles recirculate in both configurations (Fig. 3.1). The bulk of the southward particle-transport can be found just West of the WSC, extending down to 1 km (Appendix D). This exiting branch carries the Return Atlantic Water and originates from a strong eddy activity at the FS. The particles drifting within that branch later join the EGC on their way back to the South. This Return Atlantic Water extends from 5°E until the western edge of the gate in agreement with observations (Beszczynska-Möller et al., 2012) in HighRes, with the strongest signal just west of most of the positive particle-transport. It is worth noting that the Return Atlantic Water is slighly more shifted to the West in HighRes than in MedRes. In MedRes, the location of the return branch overlaps with that of the entering branch, so overall less particles (inflowing or outflowing) reach the western side of the FS. This clear east-west pattern of the particle distribution at FS is the signature of the strong recirculation occurring in HighRes in contrast with MedRes as was noted from Fig. 3.1. As a consequence, more particles join the EGC in HighRes, while particles are more prone to recirculate within the Greenland Sea in MedRes.

3.3 Origin of the Atlantic Waters at the Atlantic-Arctic gates

The branches east of 22°W make most of the contribution to the Atlantic-Arctic gates accounting for more than 95% of the particle-transport at the gates. The main and secondary pathways highlighted in Fig. 5.5a-b (Appendix E closely resemble that described in Fig. 3.1. The rest of the particle-transport at the Atlantic-Arctic gates (less than 5%) originates from the western branch of the NAC. This branch leads the particles preferably to BSO than to FS, especially in MedRes where 78% of the particles initialized west of 22°W reach BSO.

Rather than joining the Norwegian Current directly after initialization, the majority of particles first drift in the subpolar gyre before branching out towards the straits. Observations at 59.5°N show that most of the northward transport in the eastern NAC, that is east of 22°W, lie within the top 1000 m (Sarafanov et al., 2012). The eastern branch of the NAC is the most likely to merge with the Norwegian Current and transport water to the Arctic, while the western branch (west of 22°W) typically merges with the subpolar gyre circulation.

Within this top 1000 m, the first half (0-500 m) provides the bulk of the particle-transport at the gates (roughly 90% of the total transport) with an even greater predominance in MedRes (up to 95% at BSO; Fig. 3.3). It follows that waters originating from the second half ($500 - 1000$ m) contribute about 10% to the total particle-transport through the gates with a greater fraction in HighRes (9.9% to 11.7%) than in MedRes (4.8% to 8.3%). Though waters originating from below 1000 m represent only a tiny fraction ($< 1\%$) of the total particle-transport through gates in both configurations, we note that they contribute three times as more to the total particle-transport in Highres than in MedRes.

When comparing the depth origin of waters between gates, we find that FS sees a greater fraction of particle-transport carried by waters originating from between 500 m and 1000 m than BSO. To enter the very shallow Barents Sea, particles must upwell to the shelf located at a minimum depth of approximately 500 m. In contrast, particles do not need to rise as much to cross the FS, which goes down to around 4 km. Thus, particles flowing deeper than 500 m are more likely to reach FS than BSO. Particles flowing along the Norwegian shelf are generally unaffected by major topographic features along their way to FS (Fig. 3.4). However, those passing in the vicinity of the Iceland Plateau may encounter topographic obstacles, forcing them to rise in the water column before reaching FS (see some examples in Appendix H). Hence, at FS, waters crossing below 500 m may originate from any depth at 55°N as the Greenland-Iceland and Iceland-Faroe rises provide major bathymetric obstacles

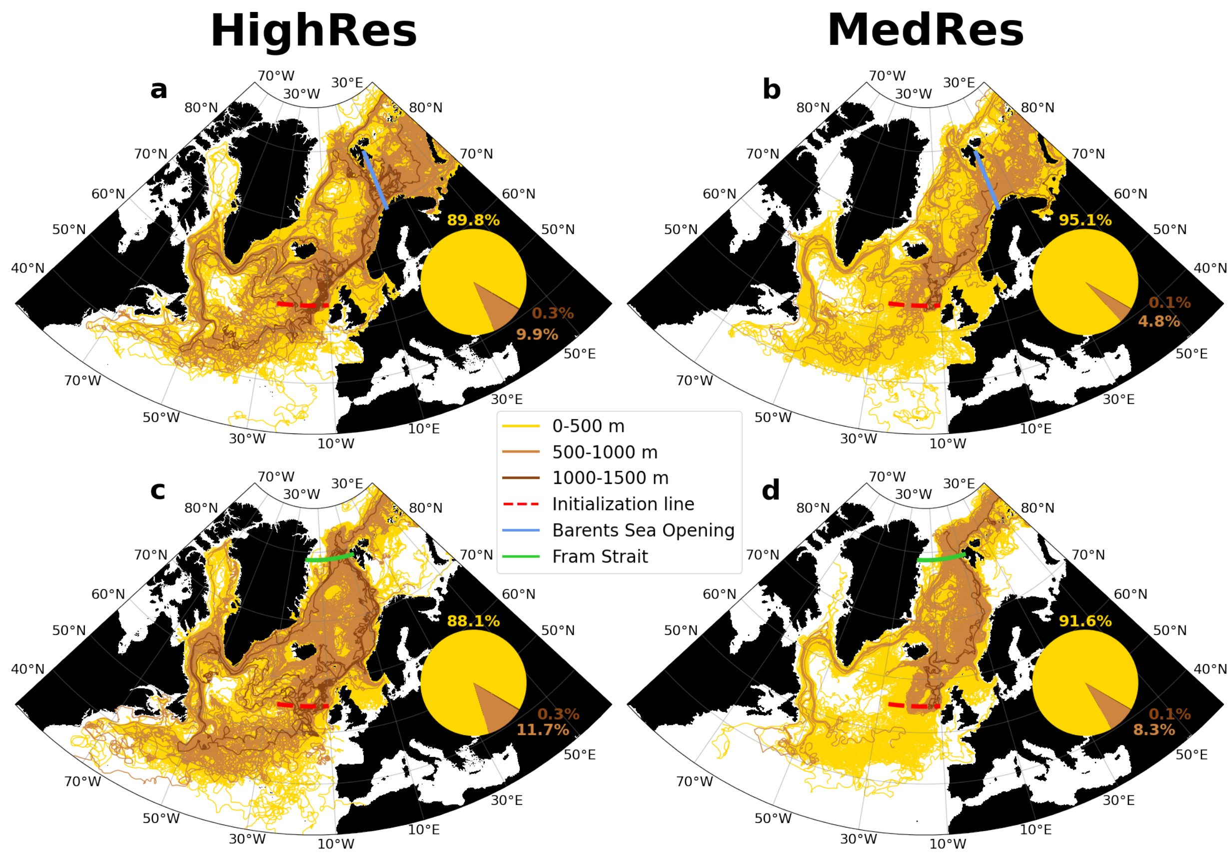

Figure 3.3: Trajectories of particles reaching (a-b) Barents Sea Opening and (c-d) Fram Strait in the two model configurations, color-coded according to their depth category at the time of initialization. For the sake of clarity, each subplot only displays 2000 trajectories, with the number of trajectories per depth range proportional to the transport distribution in that same range. Pie charts show the contribution of each depth range to the total particle-transport at each gate. Note that trajectories are flagged based on the first gate they cross. Consequently, some particles that initially reach the Barents Sea Opening might later recirculate and subsequently reach the Fram Strait, and vice versa. This explains why some trajectories crossing the Barents Sea Opening (a-b) appear to cross the Fram Strait too, and inversely for the trajectories crossing the Fram Strait (c-d).

on the road to the Atlantic-Arctic gates with maximum depth of $\sim$ 500 m.

On their way to the Atlantic-Arctic gates, intermediate and deep waters must thus rise first to pass these topographic sills before possibly sinking on their way to FS as illustrated in Fig. 3.4. We found that the deepest-initialized particles are most likely to upwell near the initialization line and continental shelves. The strongest upwelling hotspot near the

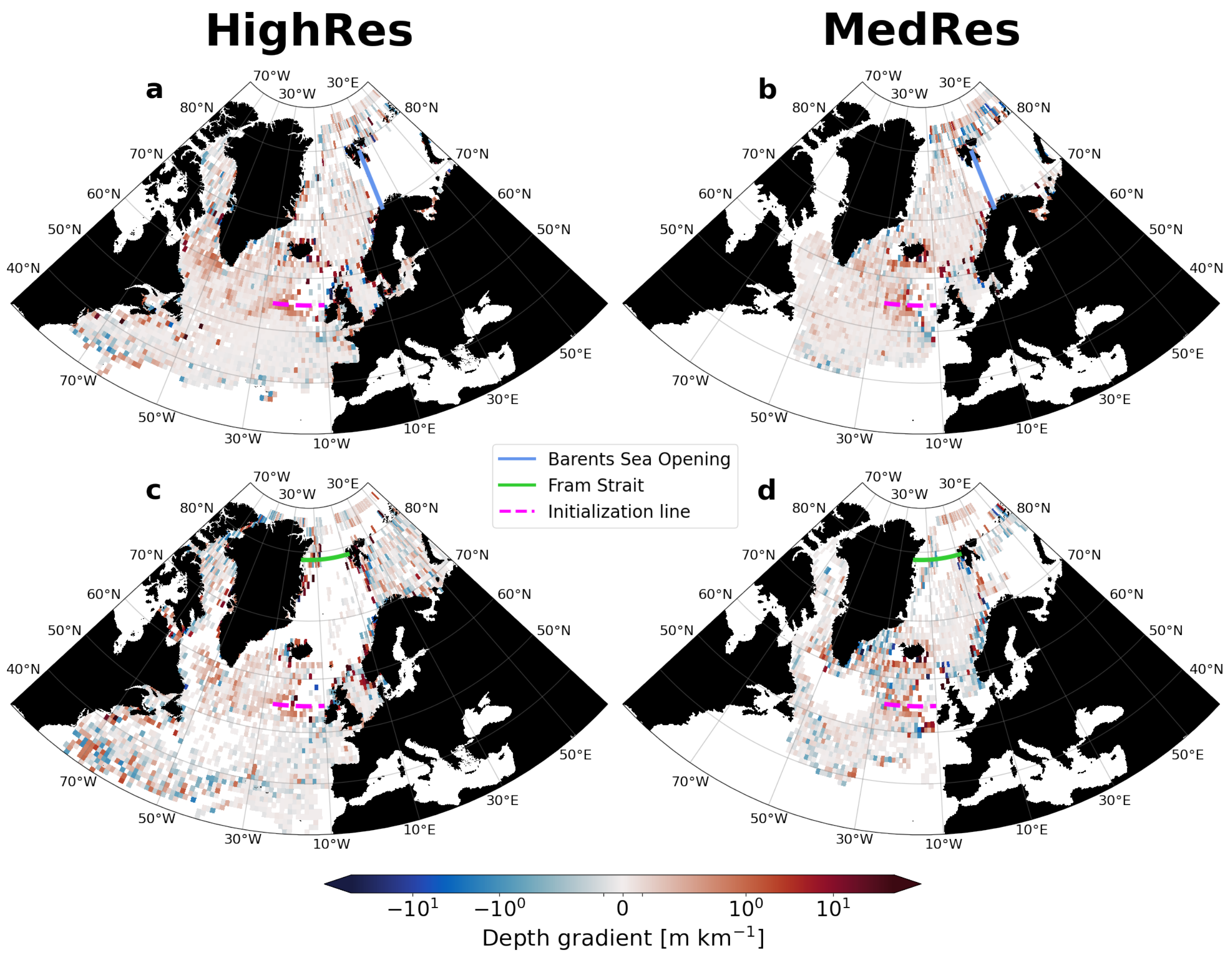

Figure 3.4: Mean depth gradient, expressed in meters vertically per kilometer horizontally, of particles initialized deeper than 1 km and reaching (a-b) Barents Sea Opening and (c-d) Fram Strait in the two model configurations. Red tints indicate upwelling (positive gradient) and blue tints indicate downwelling (negative gradient), at each 1° by 1° grid column. Note that trajectories are flagged based on the first gate they cross. Consequently, some particles that initially reach the Barents Sea Opening might later recirculate and subsequently reach the Fram Strait, and vice versa. This explains why some gradients nearby Fram Strait might be observed for the particles crossing the Barents Sea Opening first (a-b), and reciprocally for the gradients observed nearby Barents Sea Opening, for the particles crossing Fram Strait first (c-d).

initialization line appears to be around 15°W, near the Rockall Bank. At these coordinates, the Rockall Bank is less than 1 km deep and marks the separation with the Rockall Trough to the east (Fig. 2.1). This submarine bank is known to support the uplifting of water (Genin & Boehlert, 1985). On their way to BSO and FS, the majority of particles upwell directly adjacent to and all around Iceland. Additionally, particles upwell along the Norwegian coast for those crossing the BSO first, and along the Barents Sea shelf for those crossing the FS first. The continental shelves, especially the Iceland plateau, are prone to induce abrupt vertical displacements (Allen & Smeed, 1996; Trodahl & Isachsen, 2018). Compared to BSO, particles crossing FS first seem to downwell in general along the Norwegian coast and also just west of Svalbard in MedRes only. This might be the major reason why particles penetrate FS below 500 m. Interestingly, the particle-transport through FS that occurs below 500 m (see Fig. 3.2) is mostly sustained by waters originating from the top 500 m of the eastern branch of the NAC (east of 22°W; not shown). This deep transport though only represents 0.1% of the total particle-transport through FS.

3.4 Advection timescales of Atlantic Waters to the Atlantic-Arctic gates

From 55°N, particles take about 3 years on average to reach the BSO in the model configurations (Fig. 3.5a-b). This advection time agrees well with the study by Sundby and Drinkwater (2007) who showed that the great salinity anomaly of the end of the 1960s took about 2 years to reach the Barents Sea from the Faroe-Shetland region, the Faroe-Shetland region being roughly $5 - 7°$ North of our initialization line. Particles take about 1 to 1.7 additional years on average to reach FS given its more northern latitude (Fig. 3.5c-d). This advection time is in line with that of a strong temperature signal which was observed to take 1.5 years to reach FS from the Norwegian Sea (Polyakov et al., 2007). The distribution of particles' ages at time of gate crossing is slightly broader for FS compared to BSO in both configurations (Fig. 3.5a-b), with standard deviations of approximately 1.7-1.8 years for BSO and 1.9 years for FS. As illustrated in Fig. 3.1, particles may recirculate in the Norwegian Sea and the Greenland Sea before reaching either gate. These two recirculation zones are situated between BSO and FS. Consequently, particles that do not cross BSO are more likely to recirculate before crossing FS, which might slow them down and ultimately broaden their age distribution at FS.

As the model resolution is refined, the averaged travel time of particles between the initialization line and the gates is systematically reduced by 0.2 years on average at the BSO and 1 year at the FS (Fig. 3.5). In MedRes, currents tend to fade more rapidly with depth than in HighRes, a phenomenon particularly evident below 100 meters for the Norwegian

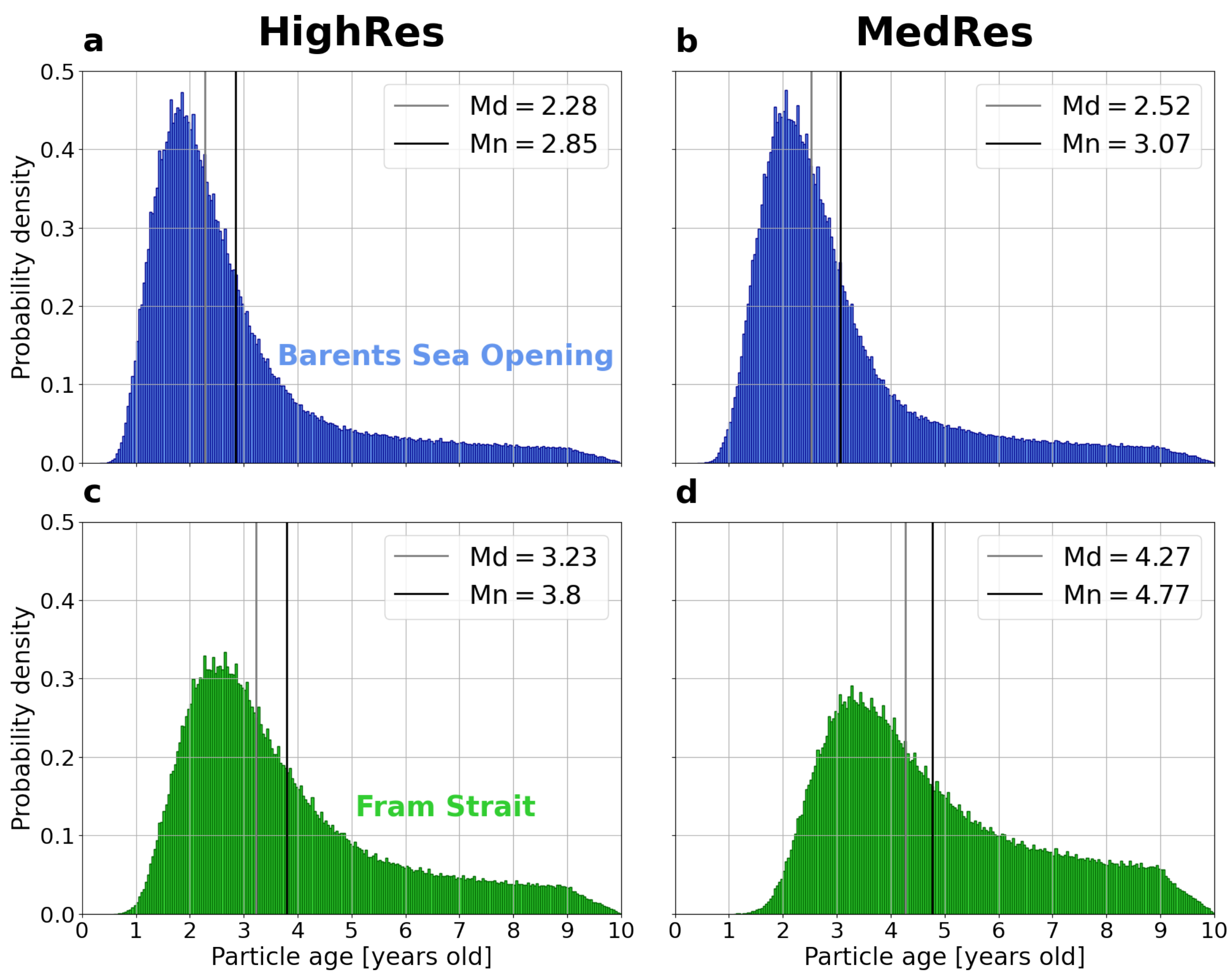

Figure 3.5: Normalized probability density distribution of the age of the particles at the time they cross a gate, for each gate and configuration. The bins size is half a month. The grey vertical line corresponds to the distribution's median (Md) and the black vertical line corresponds to the distribution's mean (Mn). Note that the abrupt decline at about 9 years is set by the advection time used for particles. However, extending the advection time to 15 years does not significantly change the mean nor the median of the distribution.

Current (Appendix F). In general, the more vigorous circulation, including stronger boundary currents, produced by HighRes compared to MedRes might explain the faster travel time of particles in the model configuration with the finer resolution. As they increased the resolution of their ocean model, Blanke et al. (2012) also found a faster connection between larvae spreading from Western to Eastern North Atlantic. Coarsening the temporal resolution of the velocity fields used for particles' advection from 5-day to monthly averaged generally yields a slower propagation of the particles at gates, except for FS in MedRes, where the mean of the distribution occurs 0.17 years before its 5-day counterpart (not shown). This slow down is in line with previous studies (e.g., Qin et al., 2014) and suggests a significant role for high frequency circulation features (such as short lived eddies, filaments, as well as storm-induced currents) to promote the advection of AW towards the Atlantic-Arctic gates.

3.5 Volume and heat transports of Atlantic Waters at the gates

3.5.1 Contribution of Atlantic Waters at 55°N to the volume and heat transports at the Atlantic-Arctic gates

From 55°N, the AW carry a total of ∼1 Sv at the Atlantic-Arctic gates in our Lagrangian experiments, corresponding to ∼15 TW (Table 2.2). The partitioning of volume and heat transports between the two main gates follow that described in Section 3.1 whereby the transport is shared about equally between BSO and FS in HighRes while about 2/3 of the transport occurs at BSO in MedRes.

It might seem surprising that in our experiment the AW only bring 10% to 20% of the positive volume transport and about 15% of the positive heat transport into the Atlantic-Arctic gates. At BSO, measurements have shown that AW contribute 62.5% and 70% of the eastward transport of volume and heat, respectively (Smedsrud et al., 2010, 2013), while at

FS, it contributes 66.7% and 49% of the northward transport of volume and heat, respectively (Schauer et al., 2004, 2008). Assuming these relative contributions of AW to the transport into the Arctic hold in our configurations, the Lagrangian estimates would actually represent $\sim 1/3$ of the inflowing AW volume and heat transports at BSO in both configurations (comparing the Lagrangian estimates with the Eulerian ones in Table 2.2). At FS, the Lagrangian estimates would represent between $\sim 1/5$ and $\sim 1/3$ of the volume and heat transports of inflowing AW in both configurations. These comparisons only provide an order of magnitude as any reference to observations should be used with caution, especially for heat transport, given that the models are run under preindustrial forcing. Further discussion on this matter is provided in Section 4.

3.5.2 Variability of volume and heat transports at the gates

In the model configurations, the annual volume transport at BSO is found to vary from ~ 0.4 to 0.7 Sv while the annual heat transport ranges from ~ 8 to 13 TW (Fig. 3.6). At FS, the interannual variability is greater in HighRes than in MedRes. While the volume transport fluctuates between ~ 0.5 and 1 Sv in HighRes, it only ranges from 0.2 to 0.5 Sv in MedRes. As for the heat transport, it fluctuates between ~ 4 and 14 TW in HighRes and between ~ 2 and 4 TW in MedRes. At both gates, the modelled ranges for volume and heat transports are found to be almost 10 times weaker than that from observations (e.g., Schauer et al., 2004; Skagseth et al., 2008). These differences might be attributed to the weaker transport values of the Lagrangian experiments exposed in the previous section.

Both volume and heat transport at the gates show higher variability in HighRes compared to MedRes, as evidenced by the systematically higher standard deviation of the time series with increased resolution (not shown). At both gates, the standard deviation increases by up to 28% for the volume transport, and by up to 74% for the heat transport when refining the resolution. HighRes is also the only configuration to show an episode of intense volume and

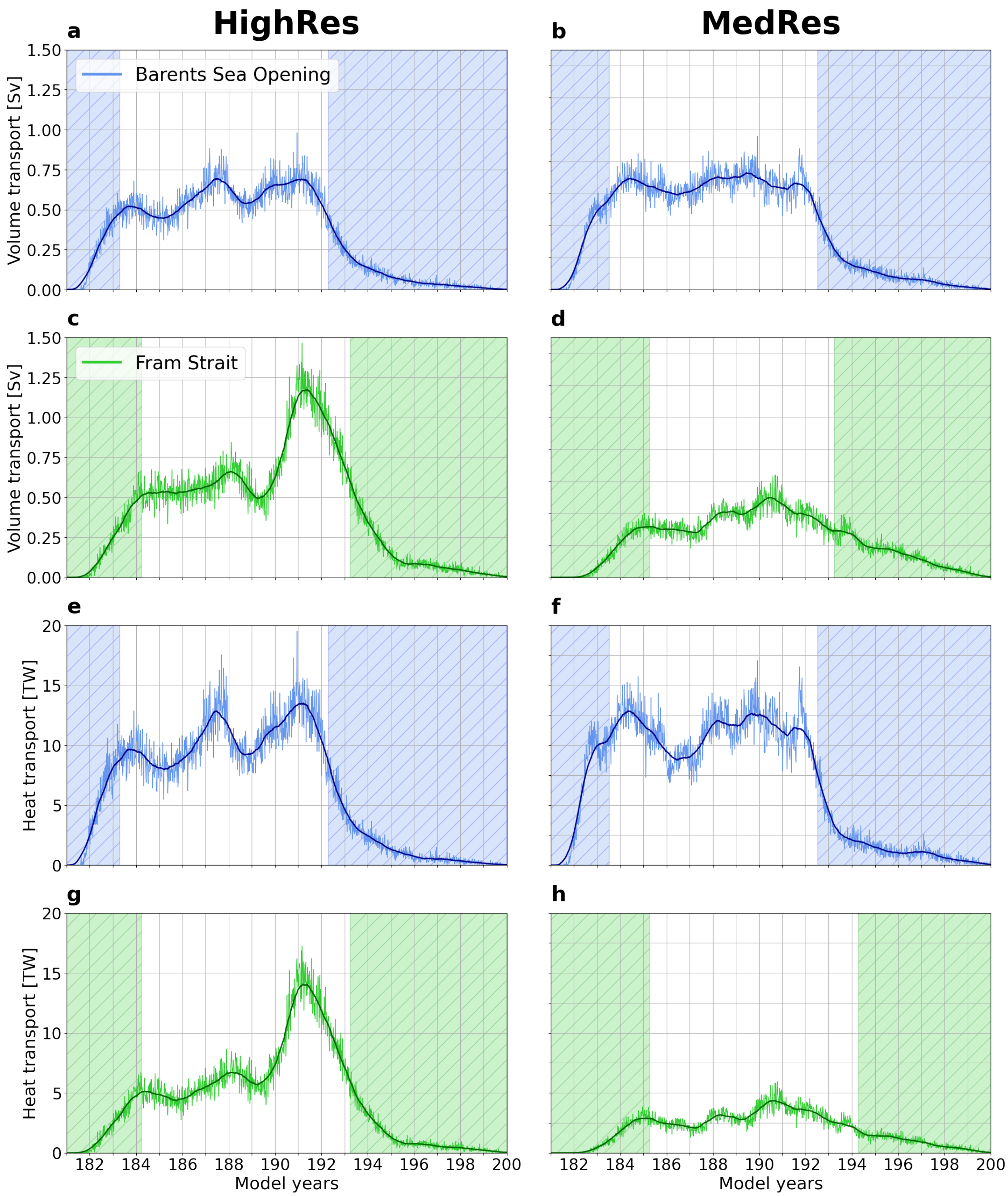

Figure 3.6: Time series of (a-d) volume transport and (e-h) heat transport across each Atlantic-Arctic gate for the entire experiment in each model configuration. Light lines show particle transport computed every 5 days, while dark lines indicate 1-year running means. White areas represent the period used to calculate the averaged transports presented in Table 2.2. This period starts by adding the median age of particles at gate crossing (Fig. 3.5) to the first experiment year (year 181) and ends by adding the median age to the last year of particle initialization (year 190).

heat transports (Fig. 3.6c-g). In the two model configurations, some episodes of high volume and heat transports occur at both BSO and FS. FS is the only gate though that shows an episode of transport exceeding 30% of the mean in HighRes (Fig. 3.6). Observations have reported on such episodes of intense transport at BSO and FS with values being 30 to 60% stronger than the mean, respectively (Schauer et al., 2004; Skagseth et al., 2008). Models have also shown pulses in heat transport that may exceeds 100% of the mean (e.g., Auclair & Tremblay, 2018).

Though FS shows an episode of intense transport during the Lagrangian experiment, BSO displays a more pronounced interannual variability in the volume and heat transports. On average, the particles crossing BSO are 2°C warmer than the ones crossing FS (Appendix G). This increased variability may be due to the fact that waters at BSO are closer to the surface, making temperatures more susceptible to fluctuations than those deeper in the water column. For volume as well as for heat, the transports at BSO and at FS show a statistically significant strong positive correlation (coefficient of up to 0.8) in both configurations (Fig. 3.6). This correlation shows that the variability of heat transport is mostly driven by that of the volume transport in agreement with Madonna and Sandø (2022) and Muilwijk et al. (2018). This strong positive correlation also suggests that the variability in the transport at both gates is controlled upstream of BSO rather than through a seesaw mechanism. In addition, this correlation illustrates the consistency of the partitioning between BSO and FS in each configuration confirming a fundamental difference in circulation between the configurations.

3.5.3 Origin of the heat pulse at Fram Strait

The highest peak in volume and heat transport occurs during year 191 at the FS in HighRes (Fig. 3.6c-g) . Before reaching this peak of roughly 1.2 Sv and 14 TW during that year, the transports were more or less constant around values of 0.6 Sv and 6 TW. Such peaks in volume and heat transport timeseries are expected as they have already been observed in both observational and modelling studies (e.g., Auclair & Tremblay, 2018; Schauer et al., 2004). Volume and heat transports have been shown to happen via pulses which can induce rapid and abrupt sea ice loss (Auclair & Tremblay, 2018). The volume and heat transports at the gates are believed to experience variations across multiple time scales, ranging from weeks to months, seasons, and years (Beszczynska-Möller et al., 2012; Skagseth et al., 2008).

While these variations might originate from several processes, the inflow through the BSO and the FS is known to be especially sensitive to storm tracks, with a particular sensitivity to the North Atlantic Oscillation (NAO) (Skagseth et al., 2008). The NAO influences both the volume and temperature of Atlantic water entering the Arctic Ocean via the Barents Sea Throughflow and the WSC (Dickson et al., 2000). In its positive phase (NAO+), characterized by high pressure over the Azores and low pressure over Iceland, the inflow of warmer Atlantic water into the Arctic basin increases (Dickson et al., 2000). In both configurations, the NAO index is found to be positively correlated to the transport in the NAC, with a significant correlation coefficient equal to 0.32 and 0.4 in HighRes and MedRes respectively (Fig. 3.7). The strongest and longest NAO+ phase occurs from late 189 until mid 193, interrupted by a short-lasting NAO- phase in mid 191. The positive correlation and timing of this NAO+ phase confirms that the highest peak in volume and heat transports at FS in HighRes is most likely due to a NAO+ phase. In MedRes, A period of prolonged NAO+ occurs from 187 until early 190. During this window, the volume and heat transports are showing pulses and are increasing accordingly too, confirming what we just stated.

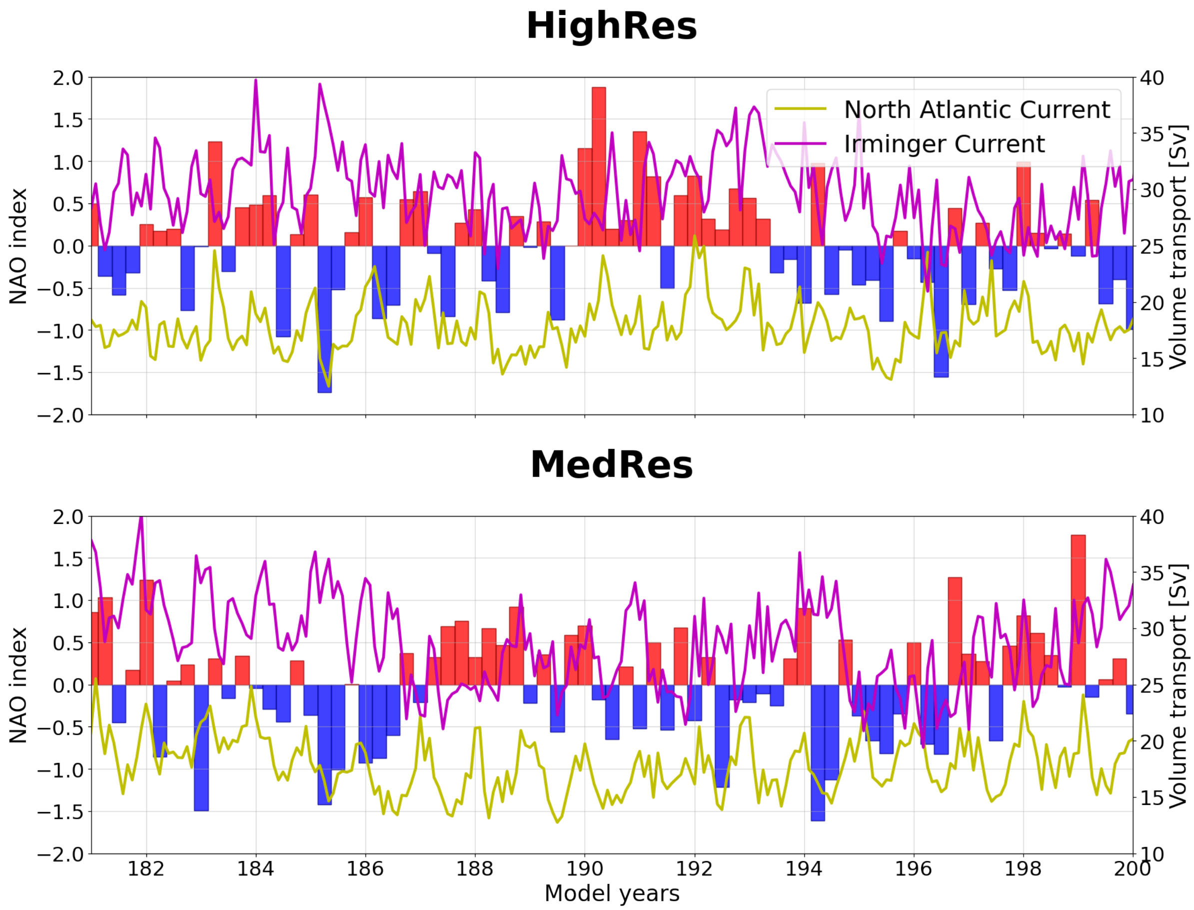

Figure 3.7: The North Atlantic Oscillation (NAO) index (red/blue; left y-axis) computed from the normalized monthly-averaged sea level pressure difference between the Azores Islands and Iceland binned seasonally for both configurations. Also depicted are the monthly averaged Eulerian northward volume transports (right y-axis) for the North Atlantic Current (yellow) and the Irminger Current (magenta).

4. Discussion and Conclusion

We conducted an offline Lagrangian tracking experiment using the medium (MedRes) and high (HighRes) resolution configurations of the CM2-O climate model suite to investigate the impact of refining horizontal resolution in the ocean component of climate models on the pathways of Atlantic Waters (AW) towards the Atlantic -Arctic gates and on their associated heat transport. Particles were initialized within the warm, salty, deoxygenated waters of the North Atlantic Current (NAC) at 55°N and tagged with a constant volume transport. Out of all the particles initialized, 6.90% and 7.08% reached the gates in HighRes and MedRes respectively, representing 11.2% and 12% of the total particle-transport initialized. Around 90% of the particle-transport crossing the gates originates from the top 500 meters of the initialization line, east of 22°W. On average, these particles reach the Atlantic-Arctic gates faster in HighRes than in MedRes, arriving ~ 0.2 years and 1 year earlier at the Barents Sea Opening (BSO) and the Fram Strait (FS) respectively. The particles that never reach one of the Atlantic-Arctic gates during the length of the experiment (10 years of advection) mainly recirculate within the subpolar gyre. Though the AW follow similar pathways towards the Arctic in the two models, significant differences appear between the two model configurations.

Upon initialization, particles follow the three main branches of the NAC, being the Rockall Passage Current, the Subarctic Front Current, and the Central Iceland Basin Current.

South of Iceland, about 50% more particle-transport bifurcates towards the west to join the Irminger Current in HighRes than in MedRes. Horizontal resolution has been shown to impact the pathway of the NAC with eddy-resolving models ($> 1/10°$) generally showing a better representation of the pathway than eddy-permitting models (Marzocchi et al., 2015; Treguier et al., 2012). Very fine resolution models ($1/20°$) were however found to overestimate the Western North Atlantic Current over the Eastern North Atlantic Current, which contrasts with observations showing the Eastern North Atlantic Current to be predominant (Breckenfelder et al., 2017). In our HighRes model, the velocity of the Western North Atlantic Current at 98.6 m depth is much stronger than in MedRes (Appendix F). The Western North Atlantic Current then feeds the Central Iceland Basin Current and East Reykjanes Current (Fig. 1.1) explaining the more vigorous Irminger Current found in HighRes. This first bifurcation of our AW on the way to the Arctic is a key difference between the two model configurations which impacts the delivery of heat to the Arctic. The more vigorous particle circulation found south of Iceland in HighRes, in line with other modelling studies (e.g., Treguier et al., 2005), leads to a higher density of particles circulating within the subpolar gyre (Fig. 3.1). When trapped in the gyre, particles take up to 5 years to make a complete loop. Some of these particles eventually find their way to the Arctic but might have lost heat as they circulate around the gyre. From the Irminger Current, 74% of the particle-transport branches off to flows around the western side of Iceland in HighRes, against 9.28% in MedRes. The greater strength of this branch in HighRes is due to the greater particle-transport in the Irminger Current. North of Iceland, the particles in HighRes then join the Norwegian Current while those in MedRes are confined within a branch flowing all around Iceland that eventually joins the subpolar gyre (Appendix F). In the subpolar gyre, 18.5% of the particle-transport enters into Baffin Bay in HighRes, against 9.59% in MedRes. The bifurcation of particles from the subpolar gyre towards the Baffin Bay is facilitated in HighRes by the better resolved West Greenland Current that allows a penetration of particles further north (Appendix F). This difference in the pathways of particles between the two model configurations leads to a difference in temperature within the Baffin Bay with HighRes showing subsurface water about 2°C than MedRes (not shown).

Within the Norwegian Sea, particles hit another major bifurcation at the entrance of BSO. While in HighRes, the majority of the particles head towards FS (55.2% of the total particle-transport across the two gates), in MedRes, the majority of the particles first reach BSO (62.1% of the total particle-transport across the two gates). The strong correlation found in the transport of volume or heat between BSO an FS show that AW have a systematic preference towards BSO or FS in each model. This bifurcation is thus likely not seesaw controlled by atmospheric forcing. In HighRes, the Norwegian Current is stronger, while in MedRes it is weaker and more diffuse throughout the top 500 m possibly favoring the penetration of particles in the Barents Sea (Appendix F). The branch detaching from the Norwegian Current and flowing into the Barents Sea is also stronger and extends over a wider range of latitudes in the top 100 m in MedRes. While the strength of the Norwegian Current might explain some of the differences between the two models, the representation of the topography might also be important in explaining these differences as a topographic ridge appears to block the way to the AW in HighRes around 14°W at BSO, while it is completely absent in MedRes (Fig. 3.2). Though the origin of the differences between the two model configurations remain unclear, flow-topography interactions may well be the lead to follow. This second bifurcation of our AW on their way to the Arctic is another key difference between the two model configurations which strongly impacts the delivery of heat to the Arctic. The heat entering at BSO is readily available to melt the sea ice over the shallow continental shelf of the Barents Sea, in contrast to the heat entering at FS which remains at depth thus isolated from the ice-covered surface. Hence, the predominance of the BSO pathway in MedRes yields a higher heat delivery to the Barents Sea that results in a reduced sea ice cover compared to HighRes as described in Decuypère et al., 2022.

The amount of heat delivered at the gates is mostly controlled by the volume transport in both configurations. Volume and heat transports show a higher variability in HighRes than in MedRes, with a standard deviation increasing by 28% and 74% for the volume and heat transports respectively when refining the resolution. In HighRes, a strong episode of heat transport, similar to heat pulses reported in the literature (Auclair & Tremblay, 2018; Holland et al., 2006; Skagseth et al., 2008), occurs in year 191 during a prolonged period of positive North Atlantic Oscillation (NAO) phase. In HighRes, the NAC is found to be positively correlated to the NAO. Hence the presence of a positive NAO phase combined with the predominance of the FS pathway for the AW in HighRes likely explain the abnormally high heat transport at FS around year 191.

Besides the differences in the AW pathways, significant differences in the contribution of the deepest AW to the transport at the Atlantic-Arctic gates also appear between model configurations. The contribution to the particle-transport across the gates of particles initialized between 500 m and 1000 m nearly doubles at BSO, and increases by 41% at FS when refining the resolution (Fig. 3.3). On their way to the Norwegian Sea, the deepest particles mainly upwell close to the European and Iceland continental shelves (Fig. 3.4). As the particles are initialized close to the Rockall Bank, most of the upwelling occurs also right after initialization. In both configurations, particles crossing BSO mainly upwell nearby the Iceland plateau, as well as along the Norwegian coast. Particles crossing FS also mainly upwell nearby the Iceland plateau, but in in contrast to BSO, they tend to sink along the Norwegian coast. Though particles seeded below 1000 m depth at 55°N hardly ever reach the Atlantic-Arctic gates (less than 1%), three times as more particles do so in HighRes than in MedRes (Fig. 3.3). Whether this greater presence of deep particles at the gates in HighRes is due to a stronger upwelling at the major topographic sills or a slow upwelling of a larger number of deep particles circulating around the gyre is yet to be determined. Furthermore, in HighRes, the northern and central branches of the NAC extend deeper throughout the water column than in MedRes (Fig. 2.1j-k), in line with observations (Daniault et al., 2016), which might also partly explain the greater contribution to particle-transport of particles originating below 1000 m.

About 10 TW of heat is found to enter the Atlantic-Arctic gates through the AW in the two model configurations. This amount of heat is worth about 1/3 of the total heat estimated to enter the gates through the AW from the Eulerian estimates. A couple of reasons might explain this difference in estimates.

First, the initialization of particles might not include all the flavors of AW. Our injection box includes most of the velocity jets carrying the warm, salty, and poorly oxygenated waters northward at 55°N (Fig. 2.1). These waters are the precursors of the AW that are known to penetrate into the Arctic through FS and BSO. At 55°N there is a northward jet at the western bound of the injection box (Fig. 2.1). This jet is not entirely included in the box in both resolutions, in MedRes there is even a very small, yet significant, jet around 30°N, outside of the injection box. However, most particles initialized west of 22°W became directly trapped within the subpolar gyre (Fig. 5.5c-d). Consequently, particles initialized in this branch and ultimately reaching the gates of interest contributed only to 4.2% of the total particle transport to the Arctic. Some jets in the initialization box also extend a bit deeper than its vertical limit (Fig. 2.1). Nevertheless, particles initialized deeper than 1 km only contributed up to 0.3% to the whole particle transport crossing the gates (Fig. 3.3). Hence, it seems that the size of the injection area might not be the main cause to explain the discrepancy between the Lagrangian and Eulerian estimates.

Second, the advection time of the particles might be relatively short to take into account all the routes towards the gates. We find that 90% of the particles take at most 7.8 years to reach one of the gates in both configurations. Yet, to test whether the advection time impacts significantly the age distribution of particles at the gates, we performed an experiment where we initialized the particles for the first 5 years and advected them for 15 years. In that experiment, 90% of the particles took at most 11.07 years to reach the gates, but the distributions' mean only shifted at most by an additional 0.3 years (not shown). Hence, the overwhelming majority of the particles still reaches the Arctic in the first couple of years of their life.

Third, the subpolar gyre and complex recirculation pattern of the Nordic Seas might delay substantially the particles on their way to the Arctic. As soon as they are injected, the majority of all the initialized particles circulate within the subpolar gyre. In both configurations, particles may take up to 5 years on average to circulate around the entire subpolar gyre. Given that our particles are tracked for 10 years, many particles might still be circulating within the gyre and could reach the gates much later than the duration of the experiment allows. Besides the subpolar gyre, recirculation of particles in the Greenland and Iceland Seas (Fig. 3.1) might also contribute to delaying their crossing of the Atlantic-Arctic gates (Huang et al., 2021).

Yet, the combination of a restrictive injection line and rather short advection time scale might explain why our Lagrangian estimates are weaker than the Eulerian estimates at the Atlantic-Arctic gates. Reconstructing the Eulerian inflow would require initializing particles across a whole latitudinal section in the North Atlantic and advecting them for more than 100 years due to the complexity of the routes towards the gates. Timescales comparable or greater than 100 years are used in multiple studies aiming to reconstruct a whole budget with offline Lagrangian tracking experiments in the Atlantic Ocean (Berglund et al., 2017; Lique & Thomas, 2018).

In conclusion, our offline Lagrangian tracking experiment highlights the critical role of model resolution in representing the pathways and associated heat transport of AW to the Arctic. The two key bifurcations, South of Iceland and at the entrance of BSO, determine heat distribution across the Atlantic-Arctic gates, ultimately impacting sea ice. Even though northward heat transport is expected to increase with resolution, accurately capturing the

AW pathways within the North Atlantic and Nordic Seas remains essential for properly representing heat distribution into the Arctic. This, in turn, is crucial for predicting changes in Arctic sea ice and enhancing our understanding of the broader climate system.

4. Bibliography

Aagaard, K., Coachman, L., & Carmack, E. (1981). On the halocline of the arctic ocean. *Deep Sea Research Part A. Oceanographic Research Papers*, *28*, 529–545. https://doi.org/10.1016/0198-0149(81)90115-1

Allen, J. T., & Smeed, D. A. (1996). Potential vorticity and vertical velocity at the iceland-færœs front. *Journal of Physical Oceanography*, *26*, 2611–2634. https://doi.org/10.1175/1520-0485(1996)026⟨2611:PVAVVA⟩2.0.CO;2

Antonov, J. I., Seidov, D., Boyer, T. P., Locarnini, R. A., Mishonov, A. V., Garcia, H. E., Baranova, O. K., Zweng, M. M., & Johnson, D. R. (2010). World ocean atlas 2009, volume 2: Salinity.

Årthun, M., Ingvaldsen, R., Smedsrud, L., & Schrum, C. (2011). Dense water formation and circulation in the barents sea. *Deep Sea Research Part I: Oceanographic Research Papers*, *58*, 801–817. https://doi.org/10.1016/j.dsr.2011.06.001

Årthun, M., & Schrum, C. (2010). Ocean surface heat flux variability in the barents sea. *Journal of Marine Systems*, *83*, 88–98. https://doi.org/10.1016/j.jmarsys.2010.07.003

Auclair, G., & Tremblay, L. B. (2018). The role of ocean heat transport in rapid sea ice declines in the community earth system model large ensemble. *Journal of Geophysical Research: Oceans*, *123*, 8941–8957. https://doi.org/10.1029/2018JC014525

Berglund, S., Döös, K., & Nycander, J. (2017). Lagrangian tracing of the water–mass transformations in the atlantic ocean. *Tellus A: Dynamic Meteorology and Oceanography*, *69*, 1306311. https://doi.org/10.1080/16000870.2017.1306311

Beszczynska-Möller, A., Fahrbach, E., Schauer, U., & Hansen, E. (2012). Variability in atlantic water temperature and transport at the entrance to the arctic ocean, 1997–2010. *ICES Journal of Marine Science*, *69*, 852–863. https://doi.org/10.1093/icesjms/fss056

Bhatt, U. S., Walker, D. A., Walsh, J. E., Carmack, E. C., Frey, K. E., Meier, W. N., Moore, S. E., Parmentier, F.-J. W., Post, E., Romanovsky, V. E., & Simpson, W. R. (2014). Implications of arctic sea ice decline for the earth system. *Annual Review of Environment and Resources*, *39*, 57–89. https://doi.org/10.1146/annurev-environ-122012-094357

Blanke, B., Bonhommeau, S., Grima, N., & Drillet, Y. (2012). Sensitivity of advective transfer times across the north atlantic ocean to the temporal and spatial resolution of model velocity data: Implication for european eel larval transport. *Dynamics of Atmospheres and Oceans*, *55-56*, 22–44. https://doi.org/10.1016/j.dynatmoce.2012.04.003

Breckenfelder, T., Rhein, M., Roessler, A., Böning, C. W., Biastoch, A., Behrens, E., & Mertens, C. (2017). Flow paths and variability of the north atlantic current: A comparison of observations and a high-resolution model. *Journal of Geophysical Research: Oceans*, *122*, 2686–2708. https://doi.org/10.1002/2016JC012444

Caesar, L., Rahmstorf, S., Robinson, A., Feulner, G., & Saba, V. (2018). Observed fingerprint of a weakening atlantic ocean overturning circulation. *Nature*, *556*, 191–196. https://doi.org/10.1038/s41586-018-0006-5

Carmack, E., Polyakov, I., Padman, L., Fer, I., Hunke, E., Hutchings, J., Jackson, J., Kelley, D., Kwok, R., Layton, C., Melling, H., Perovich, D., Persson, O., Ruddick, B., Timmermans, M.-L., Toole, J., Ross, T., Vavrus, S., & Winsor, P. (2016). Toward quantifying the increasing role of oceanic heat in sea ice loss in the new arctic. *Bulletin of the American Meteorological Society*, *96*, 2079–2105. https://doi.org/10.1175/BAMS-D-13-00177.1

Chanut, J., Barnier, B., Large, W., Debreu, L., Penduff, T., Molines, J. M., & Mathiot, P. (2008). Mesoscale eddies in the labrador sea and their contribution to convection and restratification. *Journal of Physical Oceanography*, *38*, 1617–1643. https://doi.org/10.1175/2008JPO3485.1

Chassignet, E. P., Yeager, S. G., Fox-Kemper, B., Bozec, A., Castruccio, F., Danabasoglu, G., Horvat, C., Kim, W. M., Koldunov, N., Li, Y., Lin, P., Liu, H., Sein, D. V., Sidorenko, D., Wang, Q., & Xu, X. (2020). Impact of horizontal resolution on global ocean–sea ice model simulations based on the experimental protocols of the Ocean Model Intercomparison Project phase 2 (OMIP-2). *Geoscientific Model Development*, *13*(9), 4595–4637. https://doi.org/10.5194/gmd-13-4595-2020

Claret, M., Galbraith, E. D., Palter, J. B., Bianchi, D., Fennel, K., Gilbert, D., & Dunne, J. P. (2018). Rapid coastal deoxygenation due to ocean circulation shift in the northwest atlantic. *Nature Climate Change*, *8*, 868–872. https://doi.org/10.1038/s41558-018-0263-1

Daniault, N., Mercier, H., Lherminier, P., Sarafanov, A., Falina, A., Zunino, P., Pérez, F. F., Ríos, A. F., Ferron, B., Huck, T., Thierry, V., & Gladyshev, S. (2016). The northern north atlantic ocean mean circulation in the early 21st century. *Progress in Oceanography*, *146*, 142–158. https://doi.org/10.1016/j.pocean.2016.06.007

Dawson, J., Pizzolato, L., Howell, S. E., Copland, L., & Johnston, M. E. (2018). Temporal and spatial patterns of ship traffic in the canadian arctic from 1990 to 2015 + supplementary appendix 1: Figs. s1–s7 (see article tools). *ARCTIC*, *71*, 15–26. https://doi.org/10.14430/arctic4698

Decuypère, M., Tremblay, L. B., & Dufour, C. O. (2022). Impact of ocean heat transport on arctic sea ice variability in the gfdl cm2-o model suite. *Journal of Geophysical Research: Oceans*, *127*. https://doi.org/10.1029/2021JC017762

Delandmeter, P., & van Sebille, E. (2019). The parcels v2.0 lagrangian framework: New field interpolation schemes. *Geoscientific Model Development*, *12*, 3571–3584. https://doi.org/10.5194/gmd-12-3571-2019

Delworth, T. L., Broccoli, A. J., Rosati, A., Stouffer, R. J., Balaji, V., Beesley, J. A., Cooke, W. F., Dixon, K. W., Dunne, J., Dunne, K. A., Durachta, J. W., Findell, K. L., Ginoux, P., Gnanadesikan, A., Gordon, C. T., Griffies, S. M., Gudgel, R., Harrison, M. J., Held, I. M., … Zhang, R. (2006). Gfdl's cm2 global coupled climate models. part i: Formulation and simulation characteristics. *Journal of Climate*, *19*, 643–674. https://doi.org/10.1175/JCLI3629.1

Delworth, T. L., Rosati, A., Anderson, W., Adcroft, A. J., Balaji, V., Benson, R., Dixon, K., Griffies, S. M., Lee, H.-C., Pacanowski, R. C., Vecchi, G. A., Wittenberg, A. T., Zeng, F., & Zhang, R. (2012). Simulated climate and climate change in the gfdl cm2.5 high-resolution coupled climate model. *Journal of Climate*, *25*, 2755–2781. https://doi.org/10.1175/JCLI-D-11-00316.1

Dickson, R. R., Osborn, T. J., Hurrell, J. W., Meincke, J., Blindheim, J., Adlandsvik, B., Vinje, T., Alekseev, G., & Maslowski, W. (2000). The arctic ocean response to the north atlantic oscillation. *Journal of Climate*, *13*, 2671–2696. https://doi.org/10.1175/1520-0442(2000)013⟨2671:TAORTT⟩2.0.CO;2

Docquier, D., Fuentes-Franco, R., Koenigk, T., & Fichefet, T. (2020). Sea Ice—Ocean Interactions in the Barents Sea Modeled at Different Resolutions. *Frontiers in Earth Science*, *8*. https://doi.org/10.3389/feart.2020.00172

Docquier, D., Grist, J. P., Roberts, M. J., Roberts, C. D., Semmler, T., Ponsoni, L., Massonnet, F., Sidorenko, D., Sein, D. V., Iovino, D., Bellucci, A., & Fichefet, T. (2019). Impact of model resolution on arctic sea ice and north atlantic ocean heat transport. *Climate Dynamics*, *53*, 4989–5017. https://doi.org/10.1007/s00382-019-04840-y

Docquier, D., & Koenigk, T. (2021). A review of interactions between ocean heat transport and arctic sea ice. *Environmental Research Letters*, *16*, 123002. https://doi.org/10.1088/1748-9326/ac30be

Dörr, J., Årthun, M., Eldevik, T., & Sandø, A. B. (2024). Expanding influence of atlantic and pacific ocean heat transport on winter sea-ice variability in a warming arctic. *Journal of Geophysical Research: Oceans*, *129*. https://doi.org/10.1029/2023JC019900

Dufour, C. O., Griffies, S. M., de Souza, G. F., Frenger, I., Morrison, A. K., Palter, J. B., Sarmiento, J. L., Galbraith, E. D., Dunne, J. P., Anderson, W. G., & Slater, R. D. (2015). Role of mesoscale eddies in cross-frontal transport of heat and biogeochemical tracers in the southern ocean. *Journal of Physical Oceanography*, *45*, 3057–3081. https://doi.org/10.1175/JPO-D-14-0240.1

Dunne, J. P., John, J. G., Adcroft, A. J., Griffies, S. M., Hallberg, R. W., Shevliakova, E., Stouffer, R. J., Cooke, W., Dunne, K. A., Harrison, M. J., Krasting, J. P., Malyshev, S. L., Milly, P. C. D., Phillipps, P. J., Sentman, L. T., Samuels, B. L., Spelman, M. J., Winton, M., Wittenberg, A. T., & Zadeh, N. (2012). Gfdl's esm2 global coupled climate–carbon earth system models. part i: Physical formulation and baseline simulation characteristics. *Journal of Climate*, *25*, 6646–6665. https://doi.org/10.1175/JCLI-D-11-00560.1

Fieux, M. (2017). *The planetary ocean*. EDP Sciences. https://doi.org/doi:10.1051/978-2-7598-2150-1

Ford, J. D., Pearce, T., Canosa, I. V., & Harper, S. (2021). The rapidly changing arctic and its societal implications. *WIREs Climate Change*, *12*. https://doi.org/10.1002/wcc.735

Fortin, A.-S., Dufour, C. O., Merlis, T. M., & Msadek, R. (2023). Geostrophic and mesoscale eddy contributions to the atlantic meridional overturning circulation decline under co2 increase in the gfdl cm2-o model suite. *Journal of Climate*, *36*, 6481–6498. https://doi.org/10.1175/JCLI-D-22-0561.1

Fox-Kemper, B., Danabasoglu, G., Ferrari, R., Griffies, S., Hallberg, R., Holland, M., Maltrud, M., Peacock, S., & Samuels, B. (2011). Parameterization of mixed layer eddies. iii: Implementation and impact in global ocean climate simulations. *Ocean Modelling*, *39*, 61–78. https://doi.org/10.1016/j.ocemod.2010.09.002

Frenger, I., Bianchi, D., Stührenberg, C., Oschlies, A., Dunne, J., Deutsch, C., Galbraith, E., & Schütte, F. (2018). Biogeochemical role of subsurface coherent eddies in the ocean: Tracer cannonballs, hypoxic storms, and microbial stewpots? *Global Biogeochemical Cycles*, *32*. https://doi.org/10.1002/2017GB005743

Galbraith, E. D., Gnanadesikan, A., Dunne, J. P., & Hiscock, M. R. (2010). Regional impacts of iron-light colimitation in a global biogeochemical model. *Biogeosciences*, *7*(3), 1043–1064. https://doi.org/10.5194/bg-7-1043-2010

Galbraith, E. D., Dunne, J. P., Gnanadesikan, A., Slater, R. D., Sarmiento, J. L., Dufour, C. O., de Souza, G. F., Bianchi, D., Claret, M., Rodgers, K. B., & Marvasti, S. S. (2015). Complex functionality with minimal computation: {Promise} and pitfalls of reduced-tracer ocean biogeochemistry models. *J. Adv. Model. Earth Syst.*, *7*, 2012–2028. https://doi.org/10.1002/2015MS000463

Garcia, H. E., Locarnini, R. A., Boyer, T. P., Antonov, J. I., Baranova, O. K., Zweng, M. M., & Johnson, D. R. (2010). World ocean atlas 2009, volume 3: Dissolved oxygen, apparent oxygen utilization, and oxygen saturation.

Genin, A., & Boehlert, G. W. (1985). Dynamics of temperature and chlorophyll structures above a seamount: An oceanic experiment. *Journal of Marine Research*, *43*, 907–924. https://elischolar.library.yale.edu/journal_of_marine_research/1803/

Goosse, H., Kay, J. E., Armour, K. C., Bodas-Salcedo, A., Chepfer, H., Docquier, D., Jonko, A., Kushner, P. J., Lecomte, O., Massonnet, F., Park, H.-S., Pithan, F., Svensson, G., & Vancoppenolle, M. (2018). Quantifying climate feedbacks in polar regions. *Nature Communications*, *9*, 1919. https://doi.org/10.1038/s41467-018-04173-0

Griffies, S. M., & Hallberg, R. W. (2000). Biharmonic friction with a smagorinsky-like viscosity for use in large-scale eddy-permitting ocean models. *Monthly Weather Review*, *128*, 2935–2946. https://doi.org/10.1175/1520-0493(2000)128⟨2935:BFWASL⟩2.0.CO;2

Griffies, S. M., Winton, M., Anderson, W. G., Benson, R., Delworth, T. L., Dufour, C. O., Dunne, J. P., Goddard, P., Morrison, A. K., Rosati, A., Wittenberg, A. T., Yin, J., & Zhang, R. (2015). Impacts on ocean heat from transient mesoscale eddies in a hierarchy of climate models. *Journal of Climate*, *28*, 952–977. https://doi.org/10.1175/JCLI-D-14-00353.1

Grist, J. P., Josey, S. A., New, A. L., Roberts, M., Koenigk, T., & Iovino, D. (2018). Increasing atlantic ocean heat transport in the latest generation coupled ocean-atmosphere models: The role of air-sea interaction. *Journal of Geophysical Research: Oceans*, *123*, 8624–8637. https://doi.org/10.1029/2018JC014387

Hattermann, T., Isachsen, P. E., von Appen, W.-J., Albretsen, J., & Sundfjord, A. (2016). Eddy-driven recirculation of atlantic water in fram strait. *Geophysical Research Letters*, *43*(7), 3406–3414. https://doi.org/https://doi.org/10.1002/2016GL068323

He, C., Liu, Z., & Hu, A. (2019). The transient response of atmospheric and oceanic heat transports to anthropogenic warming. *Nature Climate Change*, *9*, 222–226. https://doi.org/10.1038/s41558-018-0387-3

Heuzé, C. (2017). North Atlantic deep water formation and AMOC in CMIP5 models. *Ocean Science*, *13*(4), 609–622. https://doi.org/10.5194/os-13-609-2017

Heuzé, C., Zanowski, H., Karam, S., & Muilwijk, M. (2023). The Deep Arctic Ocean and Fram Strait in CMIP6 Models. *Journal of Climate*, *36*(8), 2551–2584. https://doi.org/https://doi.org/10.1175/JCLI-D-22-0194.1

Hjort, J., Karjalainen, O., Aalto, J., Westermann, S., Romanovsky, V. E., Nelson, F. E., Etzelmüller, B., & Luoto, M. (2018). Degrading permafrost puts arctic infrastructure at risk by mid-century. *Nature Communications*, *9*, 5147. https://doi.org/10.1038/s41467-018-07557-4

Holland, M. M., Bitz, C. M., & Tremblay, B. (2006). Future abrupt reductions in the summer arctic sea ice. *Geophysical Research Letters*, *33*. https://doi.org/10.1029/2006GL028024

Holliday, N. P., Bacon, S., Cunningham, S. A., Gary, S. F., Karstensen, J., King, B. A., Li, F., & Mcdonagh, E. L. (2018). Subpolar north atlantic overturning and gyre-scale circulation in the summers of 2014 and 2016. *Journal of Geophysical Research: Oceans*, *123*, 4538–4559. https://doi.org/10.1029/2018JC013841

Huang, J., Zhang, X., Zhang, Q., Lin, Y., Hao, M., Luo, Y., Zhao, Z., Yao, Y., Chen, X., Wang, L., Nie, S., Yin, Y., Xu, Y., & Zhang, J. (2017). Recently amplified arctic warming has contributed to a continual global warming trend. *Nature Climate Change*, *7*, 875–879. https://doi.org/10.1038/s41558-017-0009-5

Huang, J., Pickart, R. S., Bahr, F., McRaven, L. T., & Xu, F. (2021). Wintertime water mass transformation in the western iceland and greenland seas. *Journal of Geophysical Research: Oceans*, *126*. https://doi.org/10.1029/2020JC016893

Hunke, E. C., & Dukowicz, J. K. (1997). An elastic–viscous–plastic model for sea ice dynamics. *Journal of Physical Oceanography*, *27*, 1849–1867. https://doi.org/10.1175/1520-0485(1997)027⟨1849:AEVPMF⟩2.0.CO;2

Ivanov, V. V., Alexeev, V. A., Repina, I., Koldunov, N. V., & Smirnov, A. (2012). Tracing atlantic water signature in the arctic sea ice cover east of svalbard (I. N. Esau, Ed.). *Advances in Meteorology*, *2012*, 201818. https://doi.org/10.1155/2012/201818

Kurihara, Y., & Tripoli, G. J. (1976). An iterative time integration scheme designed to preserve a low-frequency wave. *Monthly Weather Review*, *104*, 761–764. https://doi.org/10.1175/1520-0493(1976)104⟨0761:AITISD⟩2.0.CO;2

Lange, M., & van Sebille, E. (2017). Parcels v0.9: Prototyping a lagrangian ocean analysis framework for the petascale age. *Geoscientific Model Development*, *10*, 4175–4186. https://doi.org/10.5194/gmd-10-4175-2017

Lannuzel, D., Tedesco, L., van Leeuwe, M., Campbell, K., Flores, H., Delille, B., Miller, L., Stefels, J., Assmy, P., Bowman, J., Brown, K., Castellani, G., Chierici, M., Crabeck, O., Damm, E., Else, B., Fransson, A., Fripiat, F., Geilfus, N.-X., ... Wongpan, P. (2020). The future of arctic sea-ice biogeochemistry and ice-associated ecosystems. *Nature Climate Change*, *10*, 983–992. https://doi.org/10.1038/s41558-020-00940-4

Large, W. G., McWilliams, J. C., & Doney, S. C. (1994). Oceanic vertical mixing: A review and a model with a nonlocal boundary layer parameterization. *Reviews of Geophysics*, *32*, 363–403. https://doi.org/10.1029/94RG01872

Lique, C., Treguier, A. M., Blanke, B., & Grima, N. (2010). On the origins of water masses exported along both sides of greenland: A lagrangian model analysis. *Journal of Geophysical Research: Oceans*, *115*. https://doi.org/10.1029/2009JC005316

Lique, C., & Thomas, M. D. (2018). Latitudinal shift of the atlantic meridional overturning circulation source regions under a warming climate. *Nature Climate Change*, *8*, 1013–1020. https://doi.org/10.1038/s41558-018-0316-5

Locarnini, R. A., Mishonov, A. V., Antonov, J. I., Boyer, T. P., Garcia, H. E., Baranova, O. K., Zweng, M. M., & Johnson, D. R. (2010). World ocean atlas 2009, volume 1: Temperature.

Madonna, E., & Sandø, A. B. (2022). Understanding differences in north atlantic poleward ocean heat transport and its variability in global climate models. *Geophysical Research Letters*, *49*. https://doi.org/10.1029/2021GL096683

Mahlstein, I., & Knutti, R. (2011). Ocean heat transport as a cause for model uncertainty in projected arctic warming. *Journal of Climate*, *24*, 1451–1460. https://doi.org/10.1175/2010JCLI3713.1

Martin, T., & Adcroft, A. (2010). Parameterizing the fresh-water flux from land ice to ocean with interactive icebergs in a coupled climate model. *Ocean Modelling*, *34*, 111–124. https://doi.org/10.1016/j.ocemod.2010.05.001

Marzocchi, A., Hirschi, J. J.-M., Holliday, N. P., Cunningham, S. A., Blaker, A. T., & Coward, A. C. (2015). The north atlantic subpolar circulation in an eddy-resolving global ocean model. *Journal of Marine Systems*, *142*, 126–143. https://doi.org/10.1016/j.jmarsys.2014.10.007

Milly, P. C. D., Malyshev, S. L., Shevliakova, E., Dunne, K. A., Findell, K. L., Gleeson, T., Liang, Z., Phillipps, P., Stouffer, R. J., & Swenson, S. (2014). An enhanced model of land water and energy for global hydrologic and earth-system studies. *Journal of Hydrometeorology*, *15*, 1739–1761. https://doi.org/10.1175/JHM-D-13-0162.1

Muilwijk, M., Smedsrud, L. H., Ilicak, M., & Drange, H. (2018). Atlantic water heat transport variability in the 20th century arctic ocean from a global ocean model and observations. *Journal of Geophysical Research: Oceans*, *123*, 8159–8179. https://doi.org/10.1029/2018JC014327

Murray, R. J. (1996). Explicit generation of orthogonal grids for ocean models. *Journal of Computational Physics*, *126*, 251–273. https://doi.org/10.1006/jcph.1996.0136

Nummelin, A., Li, C., & Hezel, P. J. (2017). Connecting ocean heat transport changes from the midlatitudes to the arctic ocean. *Geophysical Research Letters*, *44*, 1899–1908. https://doi.org/10.1002/2016GL071333

O'Garra, T. (2017). Economic value of ecosystem services, minerals and oil in a melting arctic: A preliminary assessment. *Ecosystem Services*, *24*, 180–186. https://doi.org/10.1016/j.ecoser.2017.02.024

Oldenburg, D., Armour, K. C., Thompson, L., & Bitz, C. M. (2018). Distinct mechanisms of ocean heat transport into the arctic under internal variability and climate change. *Geophysical Research Letters*, *45*, 7692–7700. https://doi.org/10.1029/2018GL078719

Oldenburg, D., Kwon, Y.-O., Frankignoul, C., Danabasoglu, G., Yeager, S., & Kim, W. M. (2024). The respective roles of ocean heat transport and surface heat fluxes in driving arctic ocean warming and sea ice decline. *Journal of Climate*, *37*, 1431–1448. https://doi.org/10.1175/JCLI-D-23-0399.1

Onarheim, I. H., Smedsrud, L. H., Ingvaldsen, R. B., & Nilsen, F. (2014). Loss of sea ice during winter north of svalbard [doi: 10.3402/tellusa.v66.23933]. *Tellus A: Dynamic Meteorology and Oceanography*, *66*, 23933. https://doi.org/10.3402/tellusa.v66.23933

Polyakov, I. V., Pnyushkov, A. V., Alkire, M. B., Ashik, I. M., Baumann, T. M., Carmack, E. C., Goszczko, I., Guthrie, J., Ivanov, V. V., Kanzow, T., Krishfield, R., Kwok, R., Sundfjord, A., Morison, J., Rember, R., & Yulin, A. (2017). Greater role for atlantic inflows on sea-ice loss in the eurasian basin of the arctic ocean. *Science*, *356*, 285–291. https://doi.org/10.1126/science.aai8204

Polyakov, I. V., Timokhov, L., Dmitrenko, I., Ivanov, V., Simmons, H., Beszczynska-Möller, A., Dickson, R., Fahrbach, E., Fortier, L., Gascard, J.-C., Hölemann, J., Holliday, N. P., Hansen, E., Mauritzen, C., Piechura, J., Pickart, R., Schauer, U., Walczowski, W., & Steele, M. (2007). Observational program tracks arctic ocean transition to a warmer state. *Eos, Transactions American Geophysical Union*, *88*, 398–399. https://doi.org/10.1029/2007EO400002

Qin, X., van Sebille, E., & Gupta, A. S. (2014). Quantification of errors induced by temporal resolution on lagrangian particles in an eddy-resolving model. *Ocean Modelling*, *76*, 20–30. https://doi.org/10.1016/j.ocemod.2014.02.002

Roberts, M. J., Hewitt, H. T., Hyder, P., Ferreira, D., Josey, S. A., Mizielinski, M., & Shelly, A. (2016). Impact of ocean resolution on coupled air-sea fluxes and large-scale climate. *Geophysical Research Letters*, *43*. https://doi.org/10.1002/2016GL070559

Rudels, B., Jones, E. P., Schauer, U., & Eriksson, P. (2004). Atlantic sources of the arctic ocean surface and halocline waters. *Polar Research*, *23*, 181–208. https://doi.org/10.1111/j.1751-8369.2004.tb00007.x

Saba, V. S., Griffies, S. M., Anderson, W. G., Winton, M., Alexander, M. A., Delworth, T. L., Hare, J. A., Harrison, M. J., Rosati, A., Vecchi, G. A., & Zhang, R. (2016). Enhanced warming of the ¡scp¿n¡/scp¿ orthwest ¡scp¿a¡/scp¿ tlantic ¡scp¿o¡/scp¿ cean under climate change. *Journal of Geophysical Research: Oceans*, *121*, 118–132. https://doi.org/10.1002/2015JC011346

Sarafanov, A., Falina, A., Mercier, H., Sokov, A., Lherminier, P., Gourcuff, C., Gladyshev, S., Gaillard, F., & Daniault, N. (2012). Mean full-depth summer circulation and transports at the northern periphery of the atlantic ocean in the 2000s. *Journal of Geophysical Research: Oceans*, *117*. https://doi.org/10.1029/2011JC007572

Schauer, U., Beszczynska-Möller, A., Walczowski, W., Fahrbach, E., Piechura, J., & Hansen, E. (2008). Variation of measured heat flow through the fram strait between 1997 and 2006. Springer Netherlands. https://doi.org/10.1007/978-1-4020-6774-7_4

Schauer, U., Fahrbach, E., Osterhus, S., & Rohardt, G. (2004). Arctic warming through the fram strait: Oceanic heat transport from 3 years of measurements. *Journal of Geophysical Research: Oceans*, *109*(C6). https://doi.org/https://doi.org/10.1029/2003JC001823

Semtner, A. J. (1976). A model for the thermodynamic growth of sea ice in numerical investigations of climate. *Journal of Physical Oceanography*, *6*, 379–389. https://doi.org/10.1175/1520-0485(1976)006⟨0379:AMFTTG⟩2.0.CO;2

Serreze, M. C., Barrett, A. P., Stroeve, J. C., Kindig, D. N., & Holland, M. M. (2009). The emergence of surface-based arctic amplification. *The Cryosphere*, *3*, 11–19. https://doi.org/10.5194/tc-3-11-2009

Sévellec, F., & Fedorov, A. V. (2016). Amoc sensitivity to surface buoyancy fluxes: Stronger ocean meridional heat transport with a weaker volume transport? *Climate Dynamics*, *47*, 1497–1513. https://doi.org/10.1007/s00382-015-2915-4

Skagseth, Ø. (2008). Recirculation of atlantic water in the western barents sea. *Geophysical Research Letters*, *35*. https://doi.org/10.1029/2008GL033785

Skagseth, Ø., Drinkwater, K. F., & Terrile, E. (2011). Wind- and buoyancy-induced transport of the norwegian coastal current in the barents sea. *Journal of Geophysical Research*, *116*, C08007. https://doi.org/10.1029/2011JC006996

Skagseth, Ø., Furevik, T., Ingvaldsen, R., Loeng, H., Mork, K. A., Orvik, K. A., & Ozhigin, V. (2008). Volume and heat transports to the arctic ocean via the norwegian and barents seas. Springer Netherlands. https://doi.org/10.1007/978-1-4020-6774-7_3

Smedsrud, L. H., Esau, I., Ingvaldsen, R. B., Eldevik, T., Haugan, P. M., Li, C., Lien, V. S., Olsen, A., Omar, A. M., Otterå, O. H., Risebrobakken, B., Sandø, A. B., Semenov, V. A., & Sorokina, S. A. (2013). The role of the barents sea in the arctic climate system. *Reviews of Geophysics*, *51*, 415–449. https://doi.org/10.1002/rog.20017

Smedsrud, L. H., Ingvaldsen, R., Nilsen, J. E. Ø., & Skagseth, Ø. (2010). Heat in the barents sea: Transport, storage, and surface fluxes. *Ocean Science*, *6*, 219–234. https://doi.org/10.5194/os-6-219-2010

Stroeve, J., & Notz, D. (2018). Changing state of arctic sea ice across all seasons. *Environmental Research Letters*, *13*, 103001. https://doi.org/10.1088/1748-9326/aade56

Sundby, S., & Drinkwater, K. (2007). On the mechanisms behind salinity anomaly signals of the northern north atlantic. *Progress in Oceanography*, *73*, 190–202. https://doi.org/10.1016/j.pocean.2007.02.002

Tamsitt, V., Drake, H. F., Morrison, A. K., Talley, L. D., Dufour, C. O., Gray, A. R., Griffies, S. M., Mazloff, M. R., Sarmiento, J. L., Wang, J., & Weijer, W. (2017). Spiraling pathways of global deep waters to the surface of the southern ocean. *Nature Communications*, *8*, 172. https://doi.org/10.1038/s41467-017-00197-0

Timmermans, M.-L., & Marshall, J. (2020). Understanding arctic ocean circulation: A review of ocean dynamics in a changing climate. *Journal of Geophysical Research: Oceans*, *125*. https://doi.org/10.1029/2018JC014378

Tooth, O. J., Johnson, H. L., Wilson, C., & Evans, D. G. (2023). Seasonal overturning variability in the eastern north atlantic subpolar gyre: A lagrangian perspective. *Ocean Science*, *19*, 769–791. https://doi.org/10.5194/os-19-769-2023

Treguier, A. M., Deshayes, J., Lique, C., Dussin, R., & Molines, J. M. (2012). Eddy contributions to the meridional transport of salt in the {North} {Atlantic}. *J. Geophys. Res.*, *117*(C5), C05010. https://doi.org/10.1029/2012JC007927

Treguier, A. M., Theetten, S., Chassignet, E. P., Penduff, T., Smith, R., Talley, L., Beismann, J. O., & Böning, C. (2005). The north atlantic subpolar gyre in four high-resolution models. *Journal of Physical Oceanography*, *35*, 757–774. https://doi.org/10.1175/JPO2720.1

Trodahl, M., & Isachsen, P. E. (2018). Topographic influence on baroclinic instability and the mesoscale eddy field in the northern north atlantic ocean and the nordic seas. *Journal of Physical Oceanography*, *48*, 2593–2607. https://doi.org/10.1175/JPO-D-17-0220.1

Tsubouchi, T., Våge, K., Hansen, B., Larsen, K. M. H., Østerhus, S., Johnson, C., Jónsson, S., & Valdimarsson, H. (2021). Increased ocean heat transport into the nordic seas and arctic ocean over the period 1993–2016. *Nature Climate Change*, *11*, 21–26. https://doi.org/10.1038/s41558-020-00941-3

van Sebille, E., Griffies, S. M., Abernathey, R., Adams, T. P., Berloff, P., Biastoch, A., Blanke, B., Chassignet, E. P., Cheng, Y., Cotter, C. J., Deleersnijder, E., Döös, K., Drake, H. F., Drijfhout, S., Gary, S. F., Heemink, A. W., Kjellsson, J., Koszalka,

I. M., Lange, M., … Zika, J. D. (2018). Lagrangian ocean analysis: Fundamentals and practices. *Ocean Modelling*, *121*, 49–75. https://doi.org/10.1016/j.ocemod.2017.11.008

van Sebille, E., Sprintall, J., Schwarzkopf, F. U., Gupta, A. S., Santoso, A., England, M. H., Biastoch, A., & Böning, C. W. (2014). Pacific-to-indian ocean connectivity: Tasman leakage, indonesian throughflow, and the role of enso. *Journal of Geophysical Research: Oceans*, *119*, 1365–1382. https://doi.org/10.1002/2013JC009525

von Appen, W.-J., Schauer, U., Hattermann, T., & Beszczynska-Möller, A. (2016). Seasonal cycle of mesoscale instability of the west spitsbergen current. *Journal of Physical Oceanography*, *46*(4), 1231–1254. https://doi.org/10.1175/JPO-D-15-0184.1

Wekerle, C., Hattermann, T., Wang, Q., Crews, L., von Appen, W.-J., & Danilov, S. (2020). Properties and dynamics of mesoscale eddies in fram strait from a comparison between two high-resolution ocean–sea ice models. *Ocean Science*, *16*, 1225–1246. https://doi.org/10.5194/os-16-1225-2020

Wekerle, C., Wang, Q., von Appen, W.-J., Danilov, S., Schourup-Kristensen, V., & Jung, T. (2017). Eddy-resolving simulation of the atlantic water circulation in the fram strait with focus on the seasonal cycle. *Journal of Geophysical Research: Oceans*, *122*(11), 8385–8405. https://doi.org/https://doi.org/10.1002/2017JC012974

Winton, M. (2000). A reformulated three-layer sea ice model. *Journal of Atmospheric and Oceanic Technology*, *17*, 525–531. https://doi.org/10.1175/1520-0426(2000)017⟨0525:ARTLSI⟩2.0.CO;2

Yamamoto, A., Palter, J. B., Dufour, C. O., Griffies, S. M., Bianchi, D., Claret, M., Dunne, J. P., Frenger, I., & Galbraith, E. D. (2018). Roles of the ocean mesoscale in the horizontal supply of mass, heat, carbon, and nutrients to the northern hemisphere subtropical gyres. *Journal of Geophysical Research: Oceans*, *123*, 7016–7036. https://doi.org/10.1029/2018JC013969

5. Appendices

A Parcels bug fix

The ocean component of the CM2-O models uses a B grid which we found was not handled properly in Parcels. More specifically, Parcels does not include the rotation of velocity fields required to account for the bipolar curvilinear grid describing the Arctic region. This led to inaccuracies in particle advection, particularly evident when particles were initialized north of Fram Strait. Instead of following the bathymetric contours, as expected, the particles exhibited unphysical trajectories (Fig. 5.1 a). To convince ourselves of the origin of the bug, we examined the possibility that the error originated from Parcels' algorithm or from biases within the model outputs. To do so, we constructed an idealized velocity field oriented eastward along constant latitudes (Fig. 5.1 b). Despite the absence of northward velocities in this field, particles still drifted northward. This is evident from their trajectories, which halted abruptly upon reaching north of 82°N. The idealized velocity field contained no data beyond this latitude.. This confirmed that the issue indeed resided within Parcels. Subsequently, we opted to define the domain in which particles evolved using the `fieldset.from_nemo()` method instead of the previously employed `fieldset.from_mom5()` method (Fig. 5.1 c). Remarkably, this adjustment yielded more realistic results, indicating that the flaw lay within the `fieldset.from_mom5()` method.

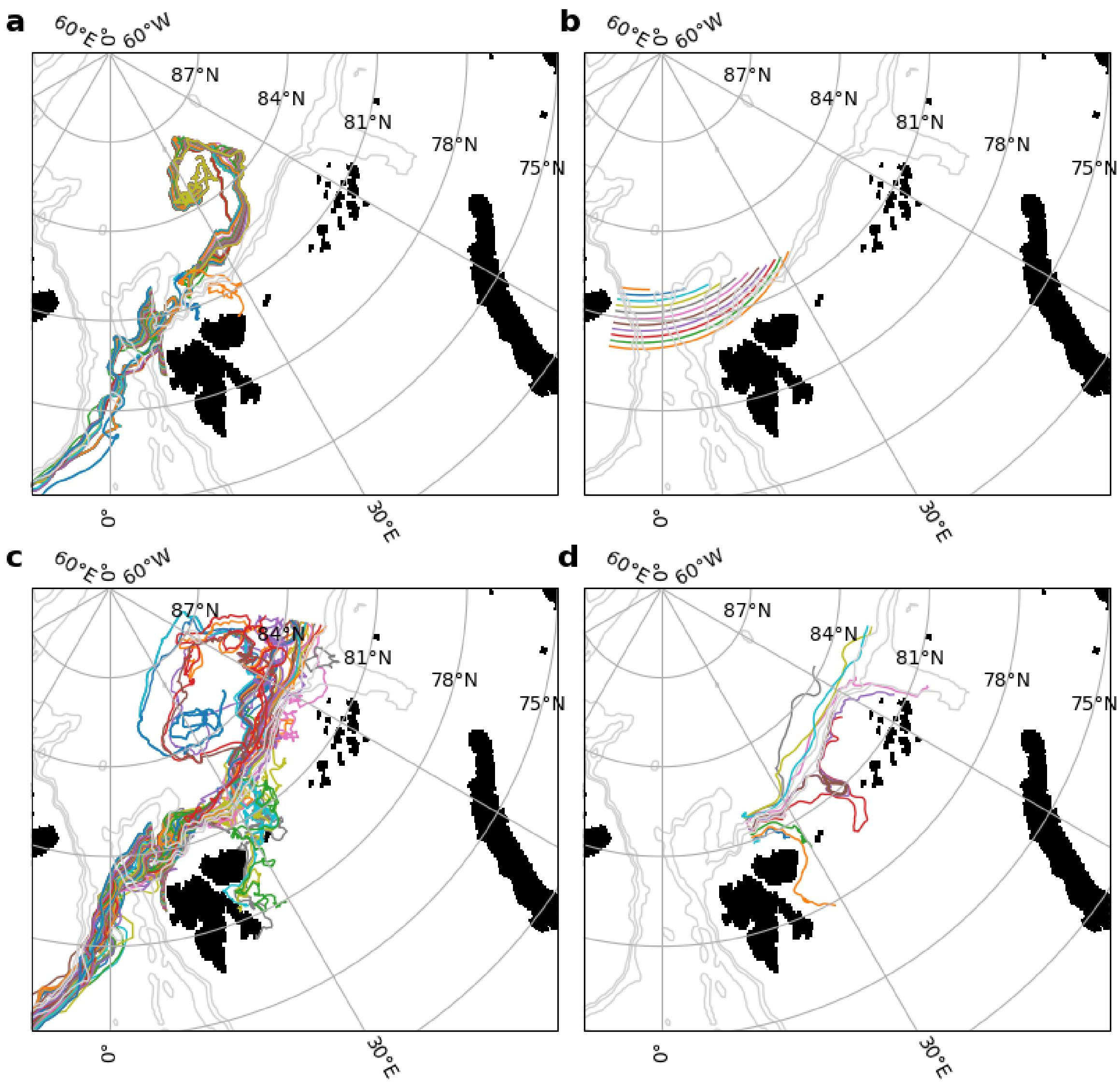

Figure 5.1: Particle trajectories initialized north of Fram Strait at the surface and advected in 2-D: a) fieldset created with from_mom5() (velocity field rotation not included), b) fieldset created with from_mom5() and particles advected with an idealized velocity field strictly following constant latitudes, c) fieldset created with from_nemo() (velocity field rotation included), d) fieldset created with from_mom5() with velocity field rotation included in a custom advection kernel (Listing 5.1). The grey lines represent the 500 m, 1 km, and 2 km isobaths in the region.

Further analysis by Prof. E. van Sebille and Dr. M. Denes, members of Parcels' development team, confirmed our findings. They identified that the rotation was not incorporated during the fieldset creation. Since fieldset.from_nemo() was intended for C grids rather than the MOM5's B grid, utilizing this method would introduce inaccuracies, potentially compromising mass conservation for example. Given the time constraints preventing a direct modification to Parcels' code, we devised a workaround. This involved developing a custom advection kernel capable of rotating the velocity field to account for the grid's curvature during particle advection (from line 8 onwards in Listing 5.1). The resulting particle trajectories are more realistic and agreed way better with our expectations (Fig. 5.1 d). The implementation details of this custom advection kernel, along with its definition, are available on GitHub under issue #1509.

```python
fset = FieldSet.from_mom5(...)

fset.add_field(Field.from_netcdf(rotfile, 'COSROT', {'lon': 'GEOLON', 'lat': 'GEOLAT'}))
fset.add_field(Field.from_netcdf(rotfile, 'SINROT', {'lon': 'GEOLON', 'lat': 'GEOLAT'}))

ROTparticle = JITParticle.add_variables({Variable('cosrot'), Variable('sinrot')})

def Rot_AdvectionRK4_3D(particle, fieldset, time): # Modified AdvectionRK4_3D Kernel to account for grid rotation
    particle.cosrot = fieldset.COSROT.eval(time, particle.depth, particle.lat, particle.lon, particle)
    particle.sinrot = fieldset.SINROT.eval(time, particle.depth, particle.lat, particle.lon, particle)

    (u1, v1, w1) = fieldset.UVW.eval(time, particle.depth, particle.lat, particle.lon, particle, applyConversion=False)

    ur1 = u1 * particle.cosrot + v1 * particle.sinrot
    vr1 = - u1 * particle.sinrot + v1 * particle.cosrot

    lon1 = particle.lon + ur1 * .5 * particle.dt / (1852. * 60. * math.cos(particle.lat * math.pi / 180.))
    lat1 = particle.lat + vr1 * .5 * particle.dt / (1852. * 60.)
    dep1 = particle.depth + w1 * .5 * particle.dt


    particle.cosrot = fieldset.COSROT.eval(time, dep1, lat1, lon1, particle)
    particle.sinrot = fieldset.SINROT.eval(time, dep1, lat1, lon1, particle)
```

```
 (u2, v2, w2) = fieldset.UVW.eval(time + .5 * particle.dt, dep1, lat1,
lon1, particle, applyConversion=False)

 ur2 = u2 * particle.cosrot + v2 * particle.sinrot
 vr2 = - u2 * particle.sinrot + v2 * particle.cosrot

 lon2 = particle.lon + ur2 * .5 * particle.dt / (1852. * 60. * math.cos
(particle.lat * math.pi / 180.))
 lat2 = particle.lat + vr2 * .5 * particle.dt / (1852. * 60.)
 dep2 = particle.depth + w2 * .5 * particle.dt


 particle.cosrot = fieldset.COSROT.eval(time, dep2, lat2, lon2,
particle)
 particle.sinrot = fieldset.SINROT.eval(time, dep2, lat2, lon2,
particle)

 (u3, v3, w3) = fieldset.UVW.eval(time + .5 * particle.dt, dep2, lat2,
lon2, particle, applyConversion=False)

 ur3 = u3 * particle.cosrot + v3 * particle.sinrot
 vr3 = - u3 * particle.sinrot + v3 * particle.cosrot

 lon3 = particle.lon + ur3 * particle.dt / (1852. * 60. * math.cos(
particle.lat * math.pi / 180.))
 lat3 = particle.lat + vr3 * particle.dt / (1852. * 60.)
 dep3 = particle.depth + w3 * particle.dt


 particle.cosrot = fieldset.COSROT.eval(time, dep3, lat3, lon3,
particle)
 particle.sinrot = fieldset.SINROT.eval(time, dep3, lat3, lon3,
```

```
    particle)

    (u4, v4, w4) = fieldset.UVW.eval(time + particle.dt, dep3, lat3, lon3,
    particle, applyConversion=False)

    ur4 = u4 * particle.cosrot + v4 * particle.sinrot
    vr4 = - u4 * particle.sinrot + v4 * particle.cosrot

    particle_dlon += (ur1 + 2*ur2 + 2*ur3 + ur4) / 6. * particle.dt /
    (1852. * 60. * math.cos(particle.lat * math.pi / 180.))  # noqa
    particle_dlat += (vr1 + 2*vr2 + 2*vr3 + vr4) / 6. * particle.dt /
    (1852. * 60.)  # noqa
    particle_ddepth += (w1 + 2*w2 + 2*w3 + w4) / 6. * particle.dt  # noqa
```

Listing 5.1: Code snippet of the custom advection kernel created to account for the curvilinearity of the MOM5 grid when advecting virtual particles with Parcels.

B Initialization schematic

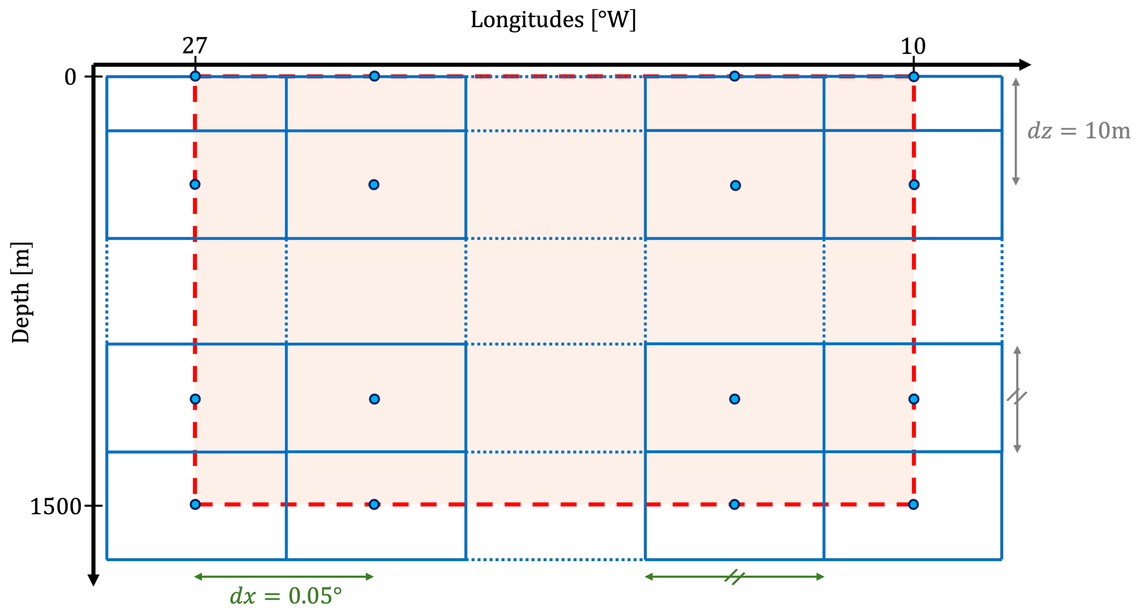

Figure 5.2: Simplified schematic of the initialization at 55°N. The virtual particles are represented with blue dots while the area attributed to each particle for the sake of computing the associated transport (*particle-transport*) is represented by the blue rectangles. The initialization area is represented by the dashed red rectangle.

C 20-year averaged velocity fields at the Atlantic-Arctic gates

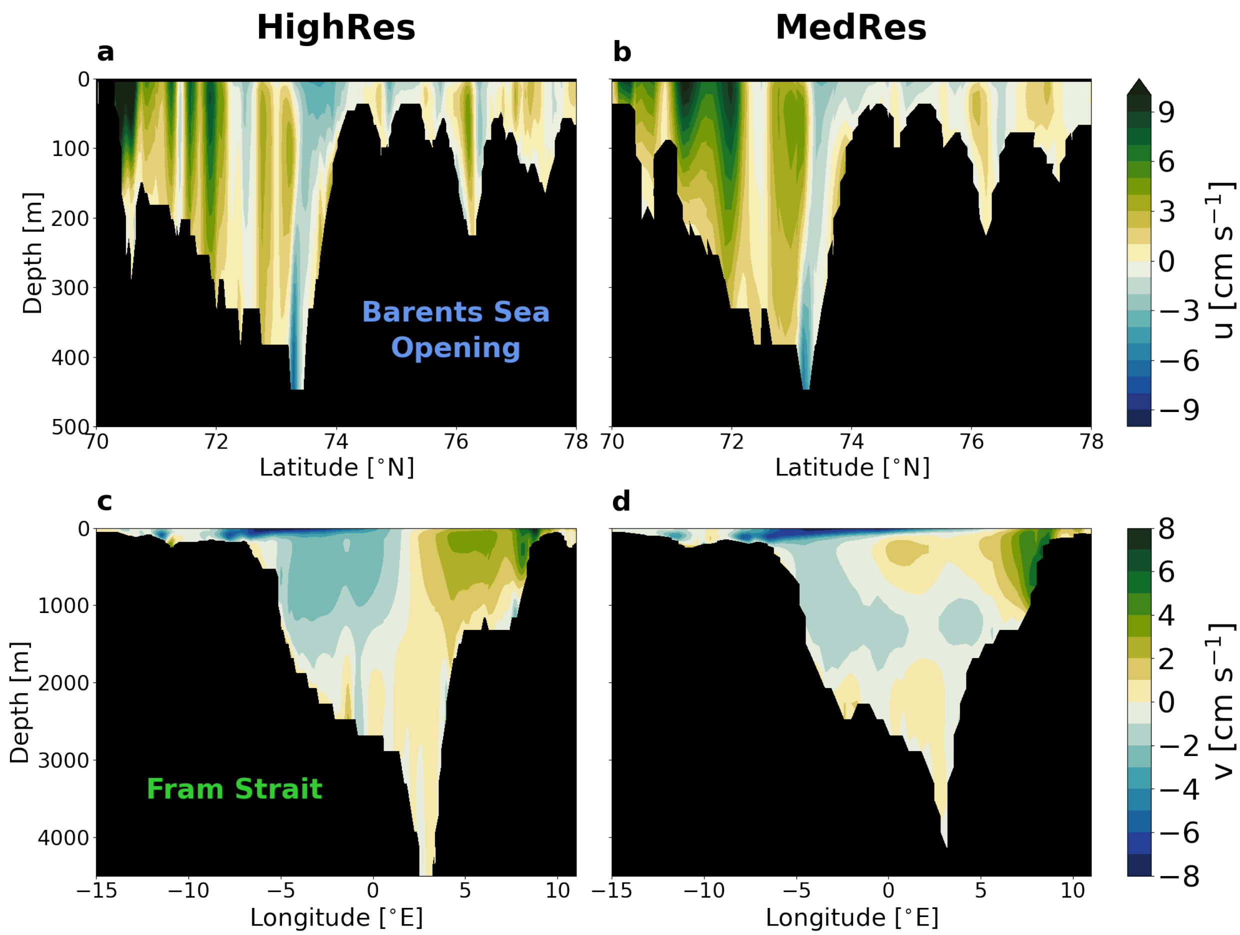

Figure 5.3: 20-year averaged (a-b) zonal (u) and (c-d) meridional (v) velocity fields at the Barents Sea Opening and Fram Strait respectively.

D Exiting transport at the Atlantic-Arctic gates

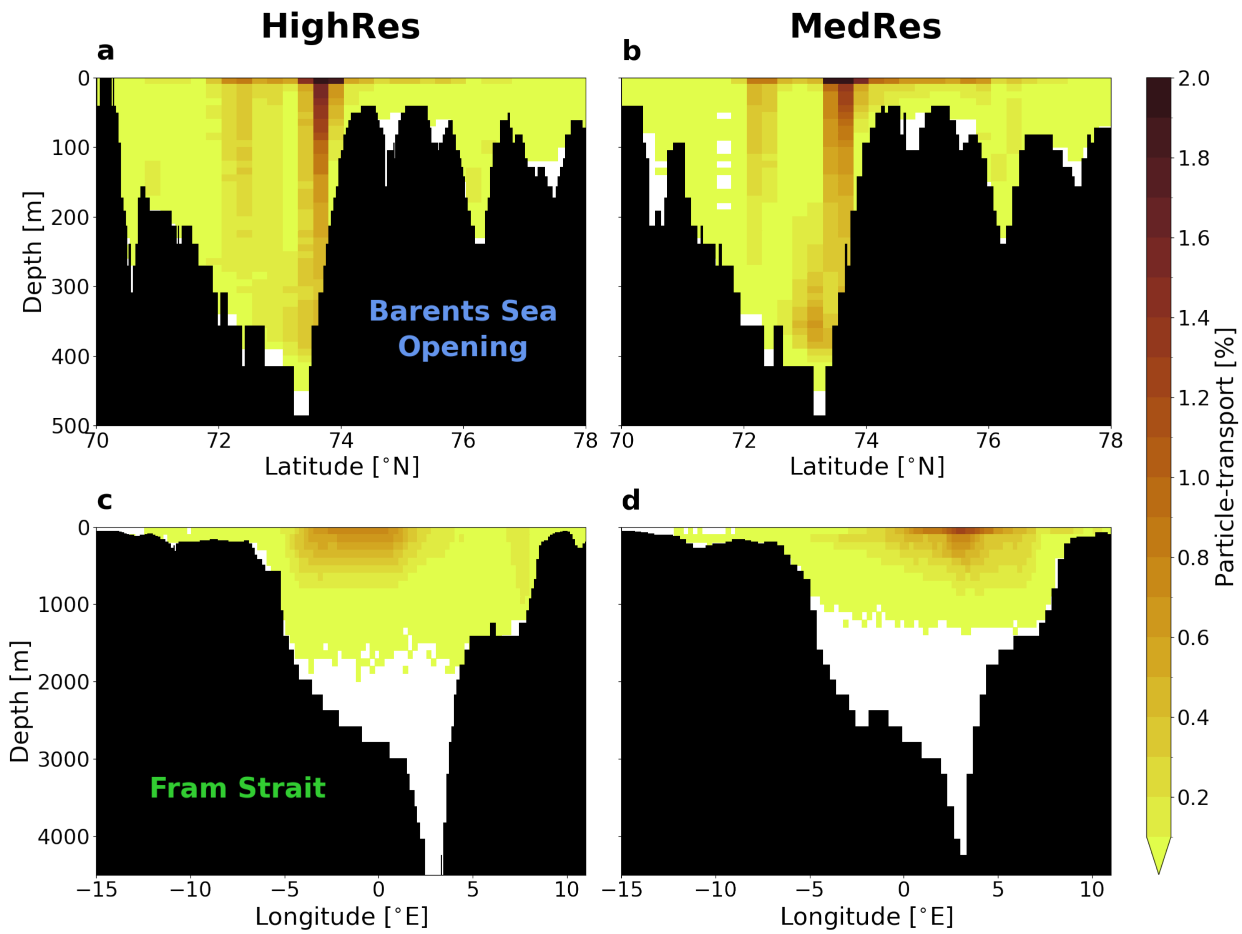

Figure 5.4: Vertical distribution of exiting particle-transport at gates. For each gate, colors indicate the fraction of particle-transport across that gate over the whole experiment. Particle-transport is binned into bins of 0.25° by 10 m for Barents Sea Opening, and 0.25° by 100 m for Fram Strait. Grid cells with high values have been visited either by many particles or by relatively fewer particles that are associated with high transport.

E Initialization branches east and west of 22°W

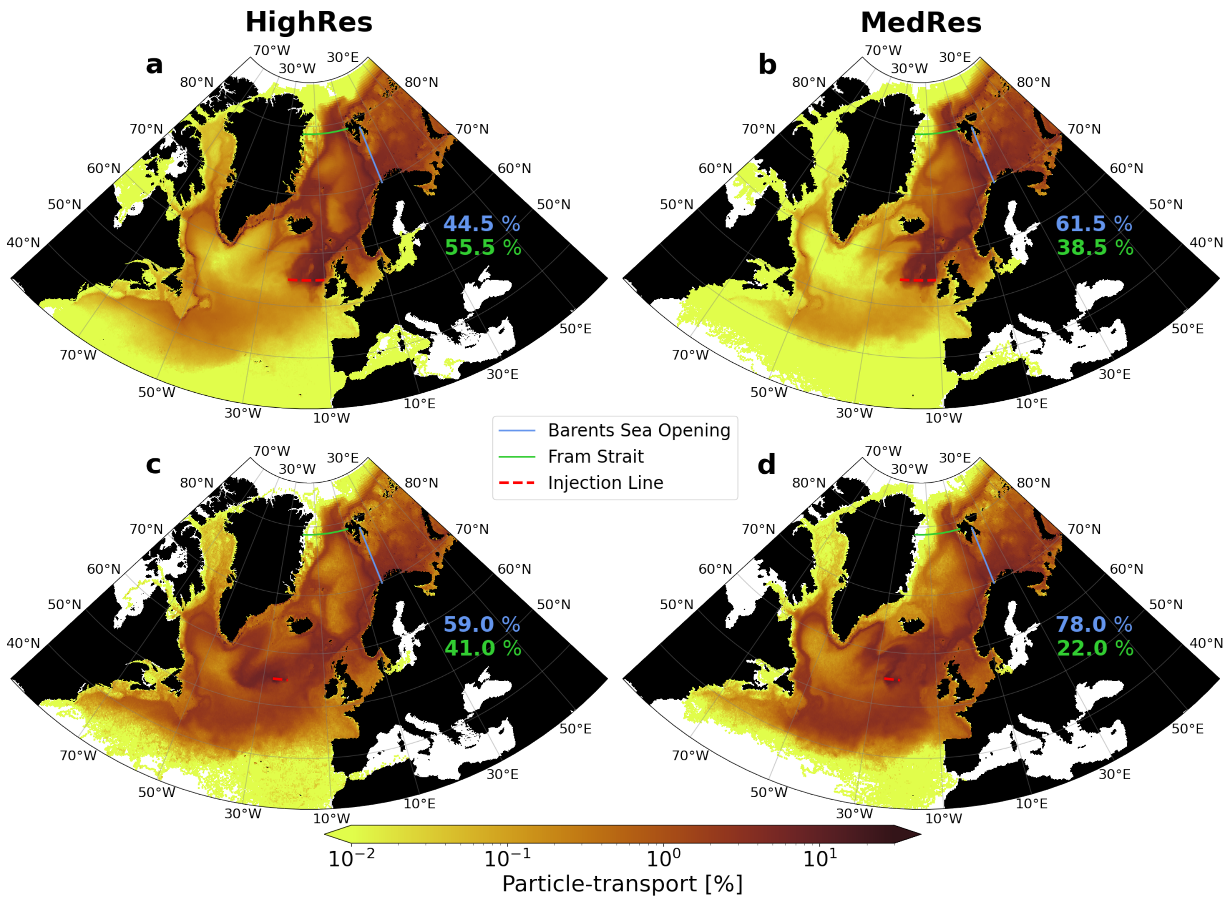

Figure 5.5: Main pathways of the particles seeded within (a-b) the eastern and (c-d) the western branch towards the Atlantic-Arctic gates and relative importance of gates. Colors indicate the fraction of the total particle transport across the Atlantic-Arctic gates (Fram Strait and Barents Sea Opening) at each 0.25° by 0.25° grid column over the whole experiment. Grid cells with high values correspond to columns which have been visited either by many particles or by relatively fewer particles that are associated with high transport. Numbers overlaid on the continent correspond to the preference of particles entering the Arctic to go through Fram Strait or Barents Sea Opening first, expressed in particle-transport and color-coded by gate.

F Velocity field at different depths in both configurations

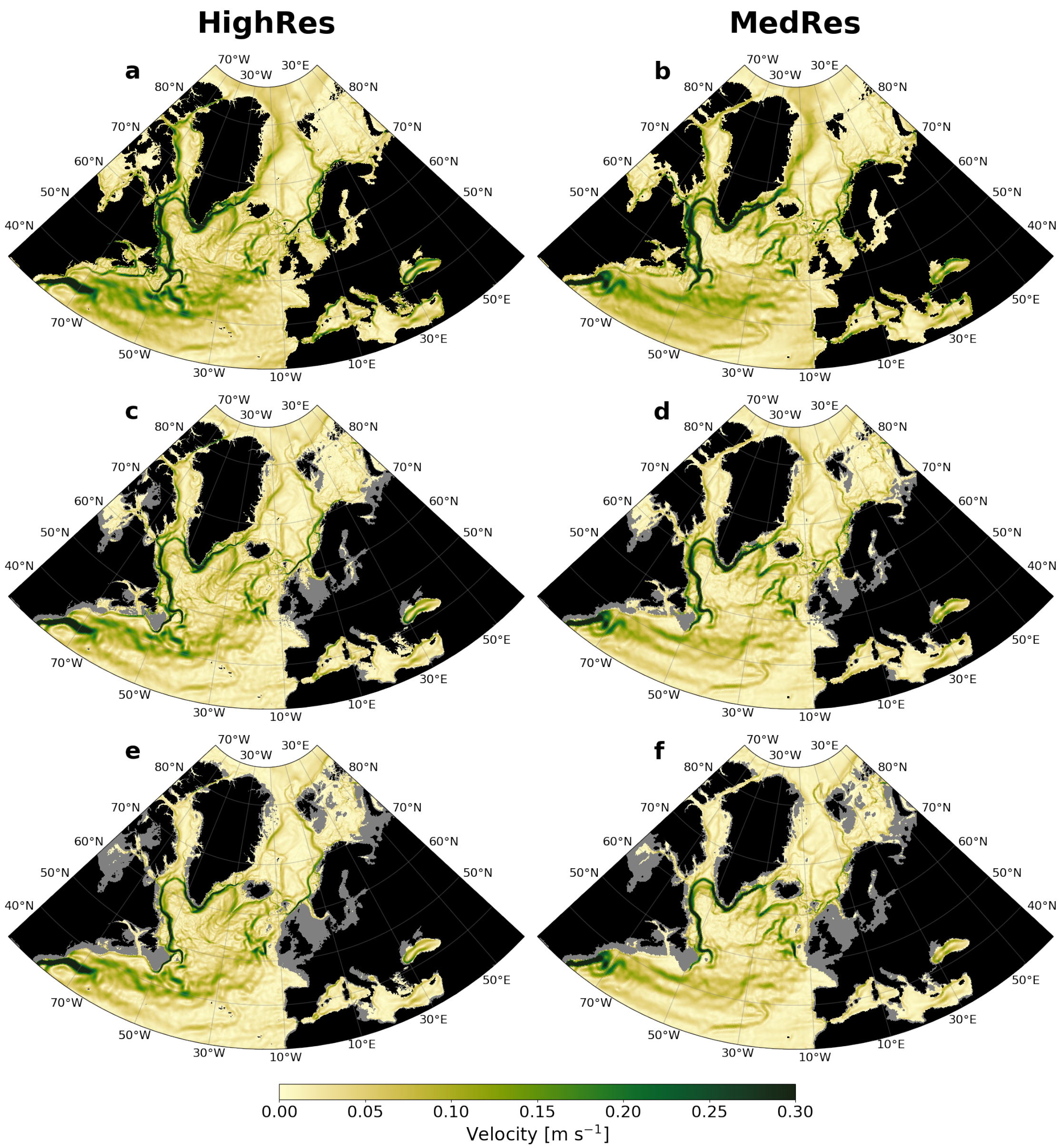

Figure 5.6: Sea velocities at (a-b) 5.03, (c-d) 98.6, and (e-f) 181 m depth in both configurations.

G Mean potential temperature timeseries

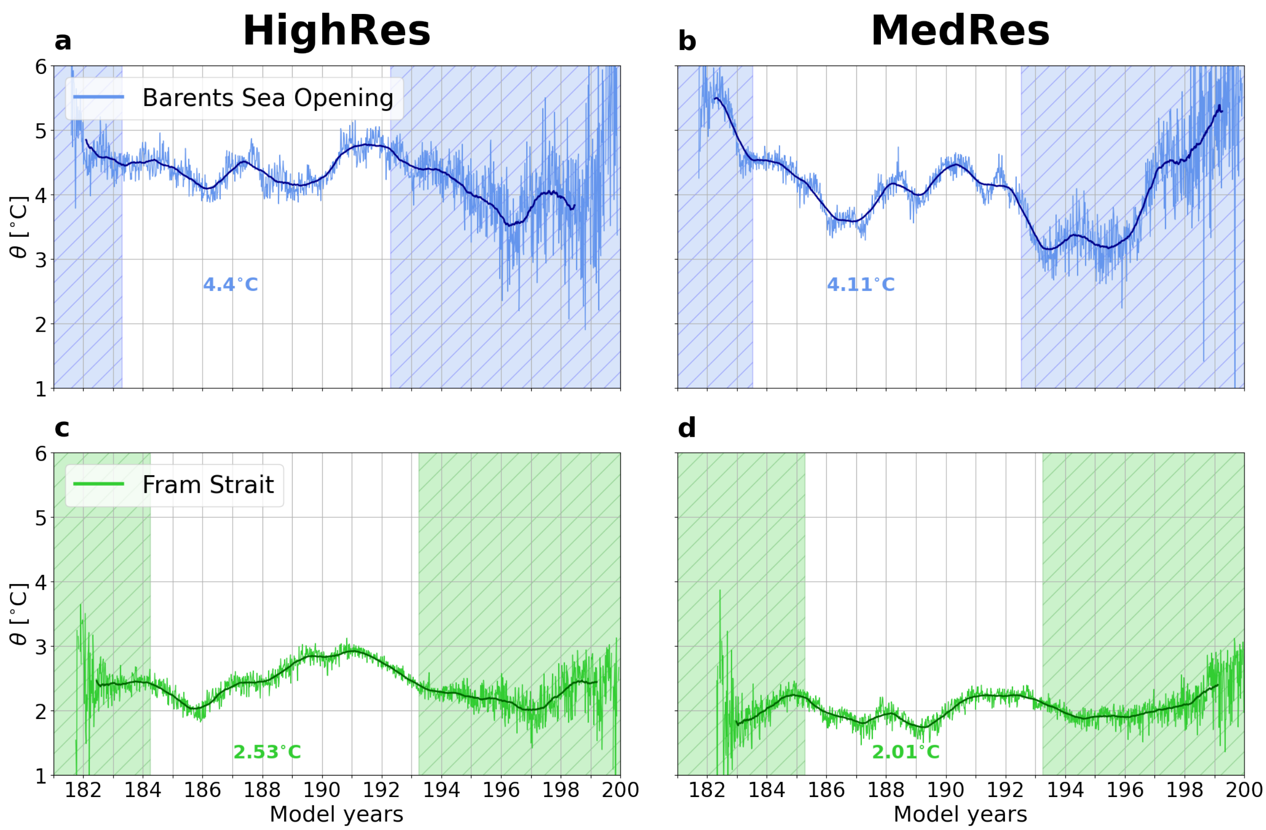

Figure 5.7: Time series of particles' mean potential temperatures when crossing (a-b) Barents Sea Opening and (c-d) Fram Strait for the duration of the entire experiment in each model configuration. Light lines represent the mean potential temperature of all particles crossing the gate during each 5-day window, while dark lines indicate the 1-year running means. White areas correspond to the periods used to calculate the average potential temperature, represented by the temperature value overlaid in each subplot. The beginning of the period is determined by adding the median of the normalized probability density distribution of the age of the particles at the time they cross a gate (Fig. 3.5) to the first year of the experiment (year 181). The end of the period is determined by adding the median to the last year of particles initialization (year 190).

H Upwelling hotspots and individual trajectories

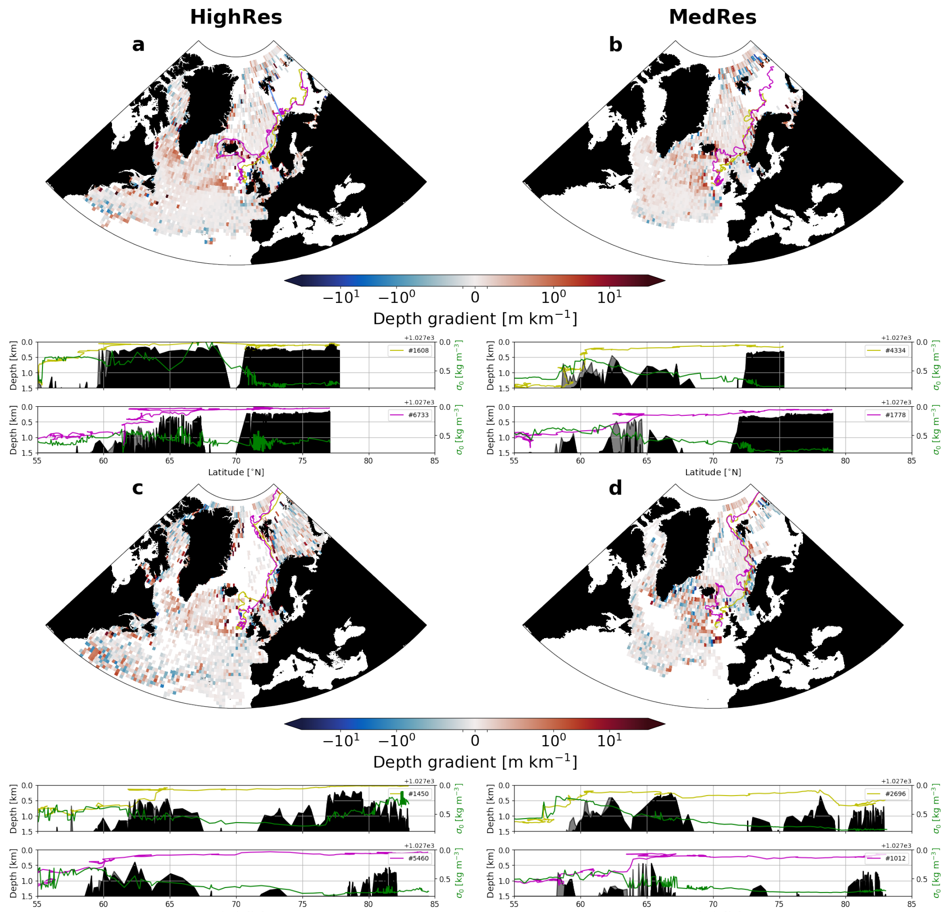

Figure 5.8: Mean depth gradient, expressed in meters vertically per kilometer horizontally, of particles initialized deeper than 1 km and reaching (a-b) Barents Sea Opening and (c-d) Fram Strait in the two model configurations. Red tints indicate upwelling (positive gradient) and blue tints indicate downwelling (negative gradient), at each 1° by 1° grid column. The two subplots below each panel show how two single particles behave in the vertical (left y-axis) throughout the latitudes during their lives (orange and magenta lines). The minimum and maximum sampled bathymetry along the particle trajectories are reprented by the black and grey areas, respectively. The green lines represent the sampled 20-years averaged potential density (σ_0) along the particle trajectories.